ACS Partner Journal
PRECISION CHEMISTRY

pubs.acs.org/PrecisionChem
Article

Compositional Complexity in High-Entropy Oxides Optimizes Colloidal Stability and Pool Boiling Heat Transfer

Published as part of Precision Chemistry special issue "Precision Chemistry for High Entropy Nanomaterials".

Keval Bharatbhai Suthar, Manjula M. Kandage, Md Moynul Hasan, Saketh Merugu, Michal Marszewski, and Anju Gupta*

Cite This: https://doi.org/10.1021/prechem.5c00360
Read Online

ABSTRACT: High-entropy oxides (HEOs) represent a class of functional materials whose interfacial chemistry and colloidal behavior remain poorly understood, limiting their development for demanding applications. This work establishes how compositional complexity in multielement oxide systems governs both colloidal stability and functional performance through a systematic investigation of eight HEO compositions in pool boiling experiments, where thermal gradients and active nucleation simultaneously test these properties under demanding conditions. Results demonstrate that HEOs with five or more equimolar elements exhibit enhanced dispersion stability compared to lower-entropy oxide systems due to configurational entropy effects, providing thermodynamic resistance to particle aggregation. Configurational entropy values of 13.38−14.90 J/mol·K exceed the critical 1.5R threshold for entropy-stabilized phases. Y-HEO, featuring yttrium combined with equimolar Co, Cr, Fe, Mn, and Ni, achieved superior performance with a 63% critical heat flux enhancement and a 135% heat transfer coefficient improvement relative to the deionized water baseline at 0.05 wt % concentration. Comprehensive surface characterization revealed that multielement oxide composition creates unique interfacial properties: contact angle reduced from 96° to 62°, minimal hysteresis of ∼12° enabling rapid rewetting, and surface roughness increased by 170%, establishing abundant nucleation sites with dramatically reduced superheat requirements. These combined effects—enhanced colloidal stability from configurational entropy, superior interfacial chemistry from compositional heterogeneity, and optimized wettability from multielement cation coordination—synergistically produced exceptional thermal performance. This work demonstrates that the precision design of multielement oxide composition directly translates fundamental materials chemistry principles into functional advantages in thermal applications.

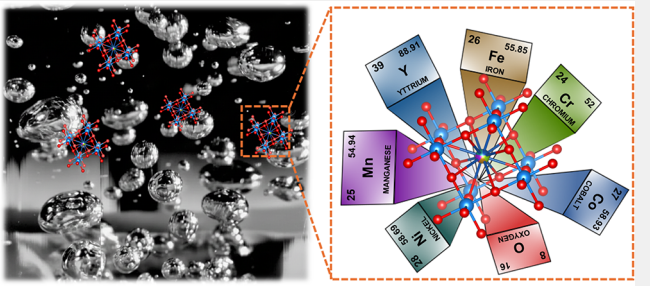

KEYWORDS: *high-entropy oxides (HEOs), configurational entropy, compositional design, colloidal stability, structure−property relationships*

1. INTRODUCTION

High-entropy oxides (HEO) represent an emerging frontier in materials chemistry, where compositional complexity at the atomic scale offers unique opportunities to engineer colloidal and interfacial behavior.[1−5] Understanding how five or more equimolar cations distributed randomly across oxide surfaces influences colloidal stability, interfacial molecular interactions, and structure−property relationships remains a fundamental challenge in precision chemistry.[6−9] While high-entropy materials have demonstrated promise in energy storage and catalysis applications,[10−13] their colloidal behavior and interfacial chemistry in dispersed systems remain poorly characterized. This gap in understanding limits the rational design of high-entropy materials for applications where suspension stability and surface properties determine functional performance. High-entropy oxide chemistry differs fundamentally from conventional materials approaches by leveraging configurational entropy as a stabilizing thermodynamic force. In traditional materials design, multielement composition often leads to phase separation and competing crystal structures as the system minimizes enthalpy. However, when five or more elements occupy equivalent lattice sites with comparable molar fractions, the configurational entropy term $T\Delta S$ becomes sufficiently large to overcome unfavorable enthalpic interactions, stabilizing a single-phase solid solution

Received: December 5, 2025
Revised: February 9, 2026
Accepted: February 10, 2026

at the atomic scale.[14−17] This entropy-driven stabilization creates materials with unprecedented compositional flexibility and tunability. Beyond the bulk crystal structure, this compositional disorder manifests in heterogeneous surface chemistry, where different metal cations occupy distinct interfacial sites, creating chemical complexity not achievable in conventional single or binary oxides.[18−22] It is hypothesized that these surface compositional effects profoundly influence interfacial molecular interactions with surrounding aqueous media, determining colloidal behavior, water structuring, hydration forces, and ultimately the stability and functionality of dispersed systems.

Characterizing how compositional complexity in HEOs translates to colloidal and interfacial properties presents significant experimental challenges. Isothermal colloidal studies[23−25] characterize stability under quasi-equilibrium conditions but fail to reveal mechanisms operating under dynamic forcing. Thermal applications provide an ideal stress test platform where extreme conditions of temperature gradients,[26−28] dynamic hydrodynamic forcing, and phase change reveal fundamental properties of dispersed high-entropy materials that remain hidden in calm dispersions. Pool boiling,[29−31] in particular, exposes colloidal systems to simultaneous demands of maintaining dispersion stability while optimizing interfacial chemistry for nucleation. The steep temperature gradients near a boiling surface exceed 10^6 K/m, creating thermophoretic forces that drive particle transport and concentration, while convective mixing from bubble nucleation maintains bulk dispersion against settling.[32−35] The phase change at the solid−liquid interface creates an extreme environment demanding precise control of wettability, contact angle behavior, and nucleation site chemistry.[36−39] These conditions directly test whether the compositional complexity of HEOs may create advantages in maintaining dispersion stability while optimizing surface interactions for nucleation. Thus, pool boiling functions as a materials characterization platform, revealing how high-entropy compositional design influences colloidal and interfacial behavior under thermal stress, providing experimental insights into structure−property relationships that precision chemistry approaches seek to establish.

Metal oxides dispersed in aqueous base fluids have shown promise as additives in pool boiling heat transfer applications, with various compositions demonstrating improvements in critical heat flux (CHF) and heat transfer coefficient (HTC).[40−44] Classical explanations associated with increased surface area and thermal conductivity[45−49] are increasingly supplemented by insights into interfacial phenomena, including particle-induced changes in surface wettability, surface roughness, and bubble dynamics.[50−52] Recent theoretical advances highlight the importance of interfacial water structure, characterized by stratification and cavitation-free energy variations, in dictating both colloidal stability and interfacial heat transfer processes.[53−57] However, existing literature often lacks a unified understanding bridging molecular-level interactions at the oxide−water interface with macroscopic boiling outcomes, particularly for high-entropy oxide systems, where compositional complexity creates qualitatively different interfacial chemistry compared to that of conventional single or binary oxides.

The present work investigates HEOs as dispersed particles in pool boiling, hypothesizing that their unique attributes—particularly high configurational entropy, multielement surface heterogeneity, and compositional tunability—generate both superior colloidal stability and enhanced interfacial chemistry for thermal applications. This study combines carefully controlled synthesis of eight high-entropy oxide compositions, advanced characterization of their structural and interfacial properties, and detailed pool boiling experiments to elucidate how compositional complexity governs both the dispersed stability and functional performance. By correlating colloidal chemistry, interfacial phenomena, and boiling heat transfer, this work provides insights into structure−property relationships in high-entropy materials while advancing fundamental understanding of how precision chemistry principles governing multielement oxide synthesis translate into functional advantages under thermal stress.

2. METHODS

2.1. HEO Synthesis and Dispersion Formation

HEOs were synthesized using a modified Pechini sol−gel method designed to ensure atomic-level mixing of constituent cations, as detailed in prior work.[58] Briefly, stoichiometric amounts of metal nitrate precursors were dissolved in deionized (DI) water and complexed with citric acid (CA) and ethylene glycol (EG) at a metal:CA:EG molar ratio of 1:3:16 to form a stable polymeric resin. This solution-based approach facilitates intimate cation mixing at the molecular level before calcination, overcoming the diffusion limitations inherent in solid-state synthesis. The precursor gel underwent drying at 110 °C, foaming, and subsequent calcination at 600 °C for 10 h to crystallize the high-entropy phase. This precision synthesis protocol yielded phase-pure crystalline powders with controlled stoichiometry. A library of 26 HEO compositions was screened for colloidal stability. Each composition was dispersed in DI water at 0.05 wt % and subjected to probe sonication at 20 kHz and 90% amplitude for 30 min to disrupt agglomerates and ensure homogeneity. Dispersion stability was assessed by time-resolved macroscopic imaging over 48 h and is provided in Figure S1 with chemical composition in Table S1 of Supporting Information (SI). Eight compositions exhibiting sedimentation resistance were selected for detailed interfacial and thermal characterization and are summarized in Table 1. While both Ti-containing and Ti-free compositions were synthesized, the present analysis focuses on the Ti-free perovskite and spinel systems, which demonstrated superior colloidal stability relevant to thermal applications.

Table 1. Chemical Composition and Crystal Structure of HEO Compositions Investigated for Colloidal Behavior

Sample Name	Chemical Formula	Crystal Structure
Al-HEO	$(Al_{1/6}Co_{1/6}Cr_{1/6}Fe_{1/6}Mn_{1/6}Ni_{1/6})_3O_4$	Spinel
La-HEO	$La(Co_{0.2}Cr_{0.2}Fe_{0.2}Mn_{0.2}Ni_{0.2})O_3$	Perovskite
Y-HEO	$Y(Co_{0.2}Cr_{0.2}Fe_{0.2}Mn_{0.2}Ni_{0.2})O_3$	Perovskite
Ce-HEO	$(Na_{0.2}K_{0.2}Ca_{0.2}La_{0.2}Ce_{0.2})TiO_3$	Perovskite
Pb-HEO	$(Sr_{0.2}Mg_{0.2}Ca_{0.2}Ba_{0.2}Pb_{0.2})TiO_3$	Perovskite
Bi-HEO	$(Na_{0.2}Bi_{0.2}Ba_{0.2}Sr_{0.2}Ca_{0.2})TiO_3$	Perovskite
K-HEO	$(K_{0.2}Ce_{0.2}Ba_{0.2}Sr_{0.2}Ca_{0.2})TiO_3$	Perovskite
Mg-HEO	$(Mg_{0.2}Co_{0.2}Ni_{0.2}Li_{0.2}Zn_{0.2})O$	Rock Salt

The working fluids used for pool boiling experiments were dilute aqueous dispersions containing 0.05 wt % HEO particles. At these low solid loadings, bulk thermophysical properties are expected to remain very close to those of

https://doi.org/10.1021/prechem.5c00360
Precis. Chem. XXXX, XXX, XXX−XXX

deionized water. Extensive literature on dilute metal oxide nanofluids consistently reports that at concentrations below 0.1 wt %, viscosity increases by less than 5%, surface tension changes by less than 3%, and thermal conductivity remains within the measurement uncertainty of the base fluid. Our recent rheological characterization of $Ti_3C_2T_x$ MXene dispersions at 0.1 wt % showed viscosity increases of only 1.4%, confirming this trend for 2D materials at dilute loadings. At the 0.05 wt % concentration used in this study, property deviations from water are expected to be even smaller. Representative values for water properties and literature data for similar dilute dispersions are compiled in Table S6 of SI.

2.2. Pool Boiling Experiment and Heater Surface Characterization

The experiments were conducted on a polished copper substrate heated from the bottom under atmospheric conditions. The surface temperature was monitored by embedded thermocouples, and the heat flux was increased in increments before the formation of a stable vapor layer signaled the onset of CHF. At each heat flux step, the difference between the temperature of the copper substrate (T_{wall}) and the saturation temperature of water (T_{sat}), known as wall superheat (ΔT_{ws}) and HTC were calculated from the measured temperature gradient through the copper chip. This approach enables benchmarking of boiling performance through two standard metrics: (i) the heat flux−ΔT_{ws} relationship and (ii) the HTC−heat flux relationship. A detailed description of the heating assembly schematic, temperature measurement scheme, and calculation steps is provided in section S2 of SI. For each working fluid, pool boiling tests were performed by increasing the applied heat flux in discrete steps until the onset of CHF. At each step, the heat input was held long enough for the wall temperature to reach a steady value and remain stable before advancing to the next level. The total boiling duration for a given test was therefore controlled by this common protocol, so that all post-boiling surfaces characterized in Section 3.5 correspond to a similar integrated thermal history for each composition rather than to distinct single flux exposures.

The copper heater surface, after pool boiling studies, was examined using a field emission scanning electron microscope acquired from JEOL, USA, to capture the deposition of HEO particles. Prior to SEM imaging, all samples were sputter-coated with a thin layer of carbon to enhance surface conductivity and minimize charging effects during electron microscopy. To obtain a clear view of HEO particles, 20 μL of the dispersion was deposited on a glass slide placed on a hot plate procured from Thermo Fisher Scientific, USA, set to 110 °C. After drying, the particles were scraped from the slide and mounted onto aluminum stubs for electron microscopy imaging. Elemental mapping was performed at an accelerating voltage of 15−25 kV using an XFlash 5010, energy-dispersive X-ray spectrometer (Bruker, USA) to confirm the HEO deposition and assess the distribution of individual metal ions. Static contact angles (SCA) of the HEO dispersions on the copper substrate were measured using an Optical Tensiometer Theta Lite purchased from Biolin Scientific, Finland, equipped with an automated sample dispenser and camera system, providing accurate measurements based on the sessile drop method. Dynamic contact angle (DCA) measurements were performed on the same equipment using DI water at 20 °C, with advancing and receding angles determined by dispensing and withdrawing the liquid at a rate of 3 μL/s over a duration of 10 s for each cycle. A VHX-600 Digital Microscope (Keyence, USA) was employed to measure the surface roughness of HEO-deposited and plain copper substrates. The same equipment was utilized to obtain clear images of the particles deposited on the glass slide for subsequent particle size distribution analysis.

3. RESULTS

This investigation approached the work from a materials chemistry perspective, where crystal structure, elemental composition, and surface chemistry represent the primary variables, with thermal performance under boiling conditions serving as a demanding validation platform for proposed colloidal mechanisms rather than the primary research focus. Eight high-entropy oxide compositions spanning three distinct crystal structures were synthesized and characterized, representing a range of compositional complexity. Dispersion stability at room temperature was assessed to establish baseline colloidal behavior under equilibrium conditions, providing a reference state for a subsequent thermal performance evaluation. Pool boiling introduced dynamic forcing conditions where steep temperature gradients, convective mixing, and phase change modify the dispersed system far from equilibrium, enabling direct experimental assessment of whether the proposed mechanisms governing HEO colloidal chemistry operate under thermal stress.

3.1. Structural Characterization and Thermodynamic Properties of HEOs

HEOs are distinguished by high configurational entropy arising from an equimolar distribution of five or more cations on equivalent crystallographic sites. Configurational entropy of mixing was calculated using the ideal solution approximation:

$$\Delta S_{mix} = -R \sum x_i \ln x_i \quad (1)$$

where R is the universal gas constant, x_i is the molar fraction of the ith cation, and the summation extends over all cation species.[22] All studied HEOs exhibit ΔS_{mix} values exceeding the 1.5R threshold, approximately 12.5 J/mol·K, which is the minimum entropic requirement for thermodynamic stabilization of single-phase solid solutions. Configurational entropy directly controls the Gibbs free energy of mixing according to:[18]

$$\Delta G_{mix} = \Delta H_{mix} - T\Delta S_{mix} \quad (2)$$

High ΔS_{mix} values overcome unfavorable mixing enthalpies at practical temperatures, enabling formation of stable multication phases. Table 2 presents calculated ΔS_{mix} values for each HEO composition, ranging from 13.38 to 14.90 J/mol·K. Structural characterization confirmed three distinct

Table 2. Configurational Entropy and Thermal Conductivity of Selected HEO Samples[a]

HEO sample	ΔS_{mix} (J/mol·K)	k (W/m·K)
Al-HEO	14.90	1.07
La-HEO	13.38	1.17
Y-HEO	13.38	1.41
Mg-HEO	13.38	3.74

[a] ΔS_{mix} calculated from equimolar cation distributions; k estimated from composite oxide models.

https://doi.org/10.1021/prechem.5c00360
Precis. Chem. XXXX, XXX, XXX−XXX

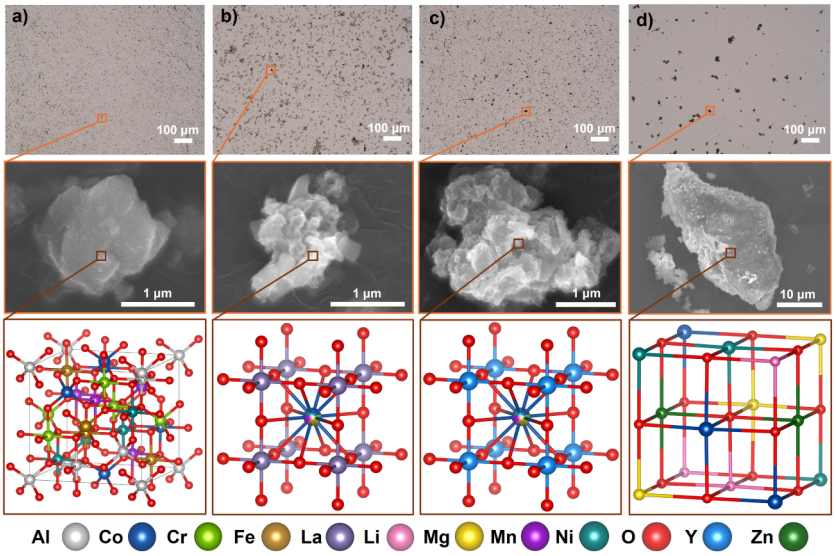

Figure 1. Multiscale characterization of selected HEO systems linking macroscopic dispersion behavior to particle morphology and crystal structure. Each row displays (top) optical micrographs of 0.05 wt % dispersions showing varying degrees of agglomeration, (middle) detailed particle morphology via FESEM revealing microstructural features, and (bottom) idealized unit cell representations illustrating the extensive cation mixing characteristic of the high-entropy phase for: a) Al-HEO (spinel), b) La-HEO (perovskite), c) Y-HEO (perovskite), and d) Mg-HEO (rock salt). Color legends denote constituent metal cations.

crystal systems represented across the HEO library: spinel (Al-HEO), perovskite (La-HEO and Y-HEO), and rock-salt (Mg-HEO), as illustrated in Figure 1. While each HEO exhibits a random spatial distribution of cations at the atomic scale, the global crystal symmetry is well-defined, indicating the successful synthesis of ordered phases despite compositional complexity. This multiscale organization of atomic disorder, coupled with long-range structural order, represents a defining characteristic of entropy-stabilized materials.

Thermal conductivity was estimated using a physics-based approach, separating electronic and phonon contributions via the Wiedemann–Franz law and kinetic theory expressions, respectively.[59,60] This methodology yielded order-of-magnitude estimates of thermal transport; more rigorous analysis would require full phonon spectrum integration and detailed scattering mechanism characterization.[61−63] However, the current approach captured the dominant thermal transport behavior within the constraints of available literature data for the constituent oxides listed in Table 2. The detailed calculation procedure for thermal conductivity is provided in Tables S2 and S3 of SI. The HEO thermal conductivity values range from 1.07 to 3.74 W/(m·K), notably lower than conventional metal oxide additives typically employed in pool boiling applications. This characteristic low thermal transport of multielement-disordered oxide systems indicates that macroscopic thermal conductivity cannot serve as the primary mechanism for any observed enhancements in boiling performance. Rather, if functional improvements emerge, they must arise from interfacial phenomena and colloidal behavior, which are investigated in subsequent sections.

3.2. Particle Morphology and Size Distribution

Particle size distribution was characterized to establish the baseline morphological properties of each HEO composition. Figure 2 displays cumulative number distributions determined from optical microscopy analysis and image processing software. The procedure adopted in this analysis along with the key statistical information is described in section S4 of the

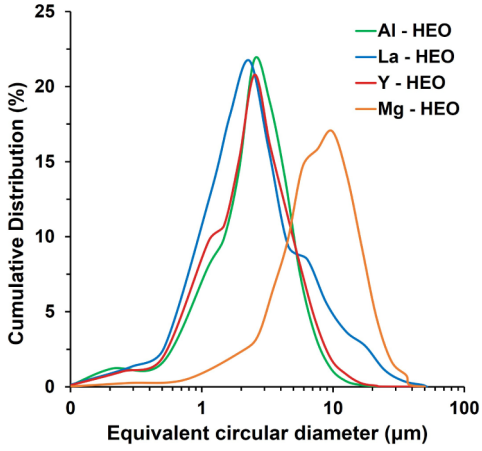

Figure 2. Particle size distribution by the equivalent circular diameter. Cumulative number distributions determined from optical microscopy for four representative HEO compositions showing median particle diameters of 2.6−3.0 μm for Al-, La-, and Y-HEO compared to a broader distribution for Mg-HEO with a median diameter of 8.1 μm (extending to ∼80 μm).

SI. Three of the HEO compositions exhibited similar median equivalent circular diameters (ECD): Al-HEO ∼2.8 μm, La-HEO ∼3.0 μm, and Y-HEO ∼2.6 μm. In contrast, Mg-HEO displayed a substantially larger median particle size of approximately 8.1 μm. Despite comparable median sizes, statistical analysis of the distributions revealed composition-dependent differences in polydispersity. Al-HEO and Y-HEO exhibited narrow, unimodal distributions with span values of approximately 1.4−1.8, characteristic of relatively uniform particle sizing. La-HEO displayed a notably broader distribution with a span of ∼3.3 and positive skewness, indicating the presence of outlier particles extending to larger diameters. Mg-HEO exhibited the broadest distribution, with a significant population of particles extending to approximately 80 μm. These compositional differences in particle sizing reflect

https://doi.org/10.1021/prechem.5c00360
Precis. Chem. XXXX, XXX, XXX−XXX

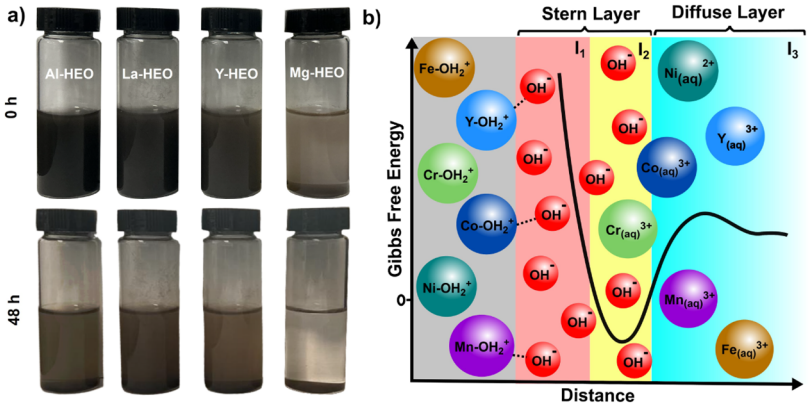

Figure 3. a) Macroscopic stability of representative HEO dispersions. Optical images of four HEO compositions dispersed at 0.05 wt % in DI water at 0 h (top) and 48 h (bottom) show varying degrees of sedimentation. Al-HEO, La-HEO, and Y-HEO exhibit minimal particles settling over 48 h at room temperature, while Mg-HEO shows more pronounced sedimentation (lighter coloration), indicating composition-dependent differences in colloidal stability. Visual assessment indicates that all four compositions maintain sufficient dispersion for thermal testing, with 0.05 wt % selected as a balance between stability and particle loading. b) Proposed schematic representation of the electrostatic double-layer structure based on classical DLVO theory and literature models for multielement oxide surfaces.

differences in synthesis conditions or particle agglomeration behavior that depend on elemental composition and crystal structure. The relationship among particle size distribution, deposition behavior during thermal cycling, and resulting surface modification is explored in subsequent sections through boiling experiments. Figure 1 provides complementary visual characterization of particle morphology at higher magnification, showing the individual particle texture and aggregate structure for each composition. While primary crystallites are nanoscale as confirmed by X-ray diffraction crystallite size analysis,[58] HEO particles exist as micrometer-scale agglomerates in aqueous dispersion, as evidenced by optical microscopy observations shown in Figures 1 and 2.

3.3. HEO Dispersion Stability

The room temperature stability of the HEO dispersions was monitored for 48 h through visual inspection and documented with high-resolution photographs, as shown in Figure 3a. The dispersions maintained good overall stability, with minor sedimentation observed in most samples and more pronounced settling in Mg-HEO. The enhanced sedimentation tendency of the Mg-HEO dispersion can be ascribed to its larger ECD relative to the other HEOs, resulting in increased gravitational settling. The uniform coloration and absence of particle aggregation indicated successful stabilization of the HEO particles in DI water. This can be attributed to combined mechanisms contributing to the long-term dispersion stability. Metal oxides typically feature −OH groups on their surface that can undergo protonation or deprotonation reactions based on the difference between the pH of the dispersion and the isoelectric point (IEP) of the sample.[64] The difference between electrostatic repulsion and attractive van der Waals (VdW) attractions determines the energy barrier that prevents particle aggregation. To estimate the IEP values of the studied HEOs, a theoretical methodology based on the individual metal oxide IEP values was adopted.[65,66] The calculated IEP values of the studied HEOs and the measured pH values of the HEO dispersions are provided in Table S5 and Figure S3 of SI. For Y-HEO, the dispersion exhibited a pH of 6.7, which was below the calculated IEP of ∼8.0, implying that the particles carry a modest positive surface charge under these conditions. This charge generates an electrical double layer (EDL) that yields moderate colloidal stability by partially counteracting VdW attractions, indicating a balance between electrostatic repulsion and attractive forces. The dispersion stability can further be supported through the Gouy−Chapman−Stern model of the EDL,[67,68] which provides a theoretical framework for ion distribution considering both electrostatic potential and thermal motion.[69−74] As illustrated in Figure 3b, the EDL consists of two distinct regions: (i) the Stern layer, where counterions are specifically adsorbed onto the charged particle surface, and (ii) the diffuse layer, where ions are distributed according to the Gouy−Chapman model under the combined influence of electrostatic forces and thermal motion.[75,76] Within the diffuse layer lies the slipping plane, which defines the hydrodynamic boundary at which the zeta potential is measured.

Recent theoretical insights[77,78] suggest that interfacial water plays a critical role in dispersion stabilization through spatially varying cavitation-free energies. The oxide−water interface creates distinct water layers:[79] (i) the I1 binding interfacial layer (BIL), where strongly bound water molecules form an ordered barrier that disfavors particle aggregation, (ii) the I2 region, characterized by enhanced density fluctuations that promote outer-sphere particle positioning, and (iii) the I3 bulk-like water region. This stratified water structure provides thermodynamic driving forces that maintain particle separation independent of surface charge effects.[80] Figure 3b depicts the proposed BIL, which contributes toward the dispersion stability of HEO particles in DI water. In the aqueous medium, due to the low ionic strength of DI water, the extended Debye length enhances long-range electrostatic interactions between particles, contributing significantly to dispersion stability.[81−84] It further depends on the adsorption behavior and aggregation resistance. Strong adsorption between dispersed particles and DI water promotes uniform suspension, while controlling surface charge and interparticle forces minimizes aggregation.[85−89] Balanced adsorption and stability ensure consistent dispersion, which is essential for reliable performance in additive-based boiling applications. Beyond classical Derjaguin−Landau−Verwey−Overbeek (DLVO) interactions,[90] structured water layers at the particle surface generate short-range hydration forces that provide additional repulsive interactions. These forces arise from the

https://doi.org/10.1021/prechem.5c00360
Precis. Chem. XXXX, XXX, XXX−XXX

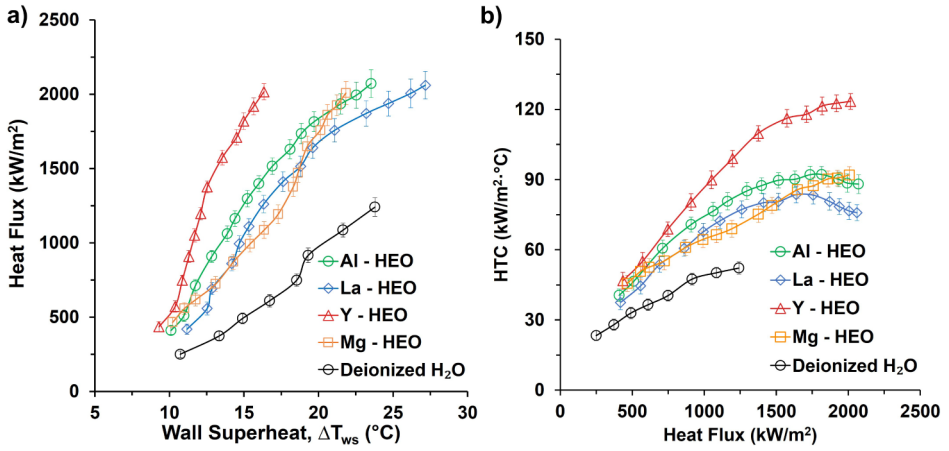

Figure 4. Pool boiling performance of four high-entropy oxide compositions compared to the DI water baseline. (a) Heat flux versus wall superheat (ΔT_{ws}). (b) HTC versus heat flux. Y-HEO exhibits superior performance with a CHF of 2017 ± 55 kW/m^2 demonstrating 63% enhancement over the baseline of 1240 ± 62 kW/m^2 and an HTC of 123 ± 3 kW/m^2·°C, a 135% improvement.

energy required to dehydrate approaching particle surfaces and become particularly important at interparticle separations below 2−3 nm. It is reported that the solution chemistry significantly influences multiple stabilization mechanisms simultaneously. pH variations alter the surface charge density and the point of zero charge, while ionic strength affects the Debye length and electrostatic screening. Importantly, these parameters also modulate interfacial water structure, creating a complex interplay between traditional DLVO forces and water network effects.[91−97]

The Brownian motion[98−100] of the dispersed HEO particles at elevated temperatures, arising from thermal fluctuations in the medium, promotes dispersion homogeneity by counteracting gravitational settling and promoting uniform distribution throughout the fluid. This thermal agitation also contributes to the dynamic nature of the diffuse double layer, where counterions continuously exchange between the particle surface and the bulk solution. The multimechanism stabilization approach is particularly advantageous for boiling heat transfer applications, where thermal and mechanical stresses can challenge colloidal stability. The redundant stabilization pathways ensure maintained dispersion integrity even under high-temperature conditions. However, in this study, this barrier was not indefinitely high, as evidenced by the eventual onset of particle settling after extended periods. Moreover, the concentration-dependent behavior reflected the competing effects of interparticle interactions and the available volume for particle motion. At low concentrations, particles had sufficient space to maintain a stable dispersion through combined electrostatic and entropic effects. However, as concentration increased, the reduced interparticle spacing intensifies attractive interactions, eventually overcoming stabilization mechanisms and leading to aggregation or phase separation.[101−103] Thus, an optimal particle concentration exists where electrostatic repulsion and configurational entropy work synergistically to maximize dispersion stability in the base fluid, providing both short-term kinetic hindrance and long-term thermodynamic resistance to aggregation.

3.4. Heat Transfer Performance and Composition-Dependent Effects

Pool boiling experiments were conducted on copper substrates to evaluate the thermal performance of four representative HEO compositions, as demonstrated in Figure 4. Heat flux was systematically increased while measuring wall superheat (ΔT_{ws}) and the corresponding HTC, yielding boiling curves that characterize the thermal response of each composition. DI water baseline provides a standard reference for evaluating the enhancement capability of HEO under atmospheric pressure pool boiling conditions on copper substrates. DI water baseline testing yielded a CHF of 1240 ± 62 kW/m^2 at a wall superheat of approximately 24 °C, consistent with literature values for pool boiling on horizontal copper surfaces at atmospheric pressure. All HEO dispersions substantially exceeded this baseline performance. Y-HEO, $Y(Co_{0.2}Cr_{0.2}Fe_{0.2}Mn_{0.2}Ni_{0.2})O_3$ achieved the highest CHF of 2017 ± 55 kW/m^2 at a wall superheat of approximately 16 °C, representing 63% enhancement over DI water. Importantly, this CHF enhancement occurred at an 8 °C lower wall temperature, indicating that multiple thermal metrics were simultaneously improved. The HTC of Y-HEO reached 123 ± 3 kW/m^2·°C, approximately 135% higher than the baseline value of 52 ± 2 kW/m^2·°C for DI water. Comparison across the four HEO compositions reveals composition-dependent performance variations. The remaining three HEO compositions achieved CHF values between 2000 and 2100 kW/m^2, while they exhibited moderate variation in their wall superheats and HTC, as evident from the thermal performance chart. These differences, despite all compositions exceeding baseline performance, indicate that elemental composition and the resulting crystal structure influence the thermal response. Figure 4 shows the complete boiling curves for all four compositions. Figure 4a reveals CHF capability and wall superheat requirements, while Figure 4b shows sustained HTC performance across varying heat flux conditions, demonstrating that HEO enhancements persist across the full boiling regime, not merely at maximum conditions. HEO dispersions consistently achieved higher heat flux at lower wall superheat compared to baseline DI water across the full operating range, not solely at CHF conditions. Error bars indicate ±1 standard deviation of n = 3 replicate measurements.

3.5. Post-Boiling Surface Characterization

The copper substrates exposed to HEO dispersions during pool boiling underwent dramatic modifications to their surface topography, chemistry, and interfacial energetics. These changes represent direct manifestations of HEO particle deposition and provide critical insights into the mechanisms

https://doi.org/10.1021/prechem.5c00360
Precis. Chem. XXXX, XXX, XXX−XXX

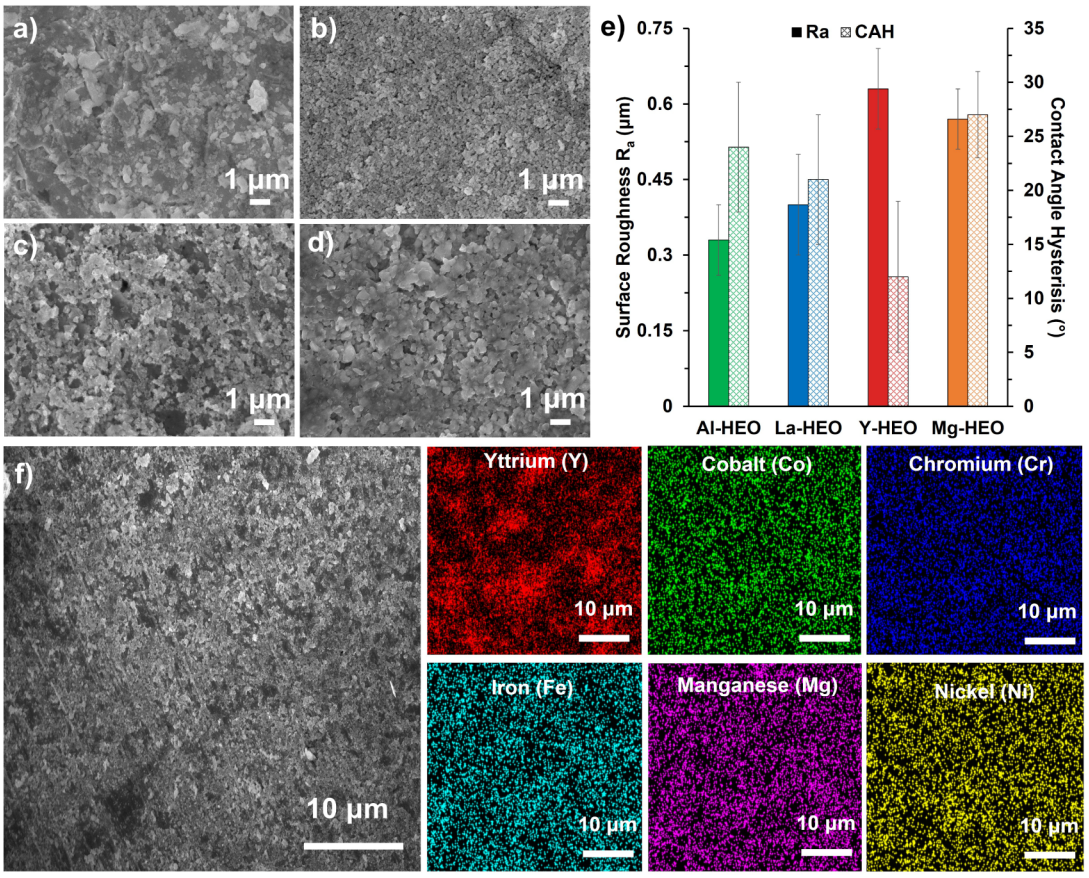

Figure 5. Surface characterization of HEO-modified copper substrates. (a-d) FESEM micrographs showing the textured particle deposition layer: (a) Al-HEO, (b) La-HEO, (c) Y-HEO, and (d) Mg-HEO. (e) Quantitative surface metrics comparing arithmetic average roughness (Ra) and contact angle hysteresis (CAH). Y-HEO exhibits a unique combination of high roughness (Ra ≈ 0.63 μm) for nucleation and low hysteresis (~12°) for efficient liquid rewetting, distinguishing it from other compositions. (f) Elemental mapping of the Y-HEO sample deposited on the copper substrate.

governing the observed heat transfer enhancements. Systematic characterization, combining scanning electron microscopy, energy-dispersive X-ray spectroscopy, surface roughness analysis, and DCA measurements, reveals how compositional complexity in HEOs translates to controlled surface modifications that optimize thermal performance. Scanning electron microscopy of the post-boiling copper substrates revealed composition-dependent variations in the deposited particle layer morphology. The pristine copper baseline exhibited the characteristic smooth surface of mechanically polished metal, with oriented scratch marks from the 600-grit polishing process creating modest surface roughness of Ra = 0.23 ± 0.06 μm. This polished state provided a uniform but relatively featureless substrate with limited inherent nucleation cavities. Following boiling with HEO dispersions, all four compositions produced textured surface coatings distinctly different from those of the baseline. Al-HEO deposition generated a moderately rough surface with Ra = 0.33 ± 0.07 μm, representing a 43% increase over the baseline. La-HEO produced intermediate roughness of Ra = 0.40 ± 0.10 μm, showing 74% increase. Mg-HEO achieved Ra = 0.57 ± 0.06 μm with a 148% increase. Y-HEO exhibited the most pronounced surface modification with Ra = 0.63 ± 0.08 μm, corresponding to a 174% increase in roughness compared with the pristine substrate. The SEM micrographs shown in Figure 5a–d demonstrate that Y-HEO created a denser, more uniformly textured deposition layer compared to the other compositions, with surface features appearing more finely resolved and densely packed. This composition-dependent variation in deposition quality from sparse, scattered particles of Al-HEO to dense, well-packed texturing by Y-HEO indicates that elemental composition influences particle adhesion characteristics and packing efficiency during the transient deposition process in boiling. The high roughness achieved by Y-HEO suggests superior particle–substrate interaction or optimal particle morphology for dense packing, creating abundant potential nucleation sites per unit area.[104−106] The measured reduction in wall superheat can be interpreted in terms of the range of nucleation site sizes that are activated on each surface. Using the classical relationship between the cavity radius and required superheat given in eq 4, the experimental values of ΔT_{ws} imply characteristic cavity radii in the micrometer range for both the baseline copper and the HEO-modified surfaces. These inferred cavity dimensions are consistent with the size of surface asperities and particle clusters observed in the SEM images, indicating that HEO deposition creates a dense population of cavities that are thermodynamically favorable for nucleation under the present conditions.

DCA analysis quantified the effects of HEO deposition on the modification of the interfacial energetics, further governing liquid–surface interactions[107,108] during boiling. This characterization was particularly important for understanding bubble dynamics, as the ease with which liquid rewetted the heated

https://doi.org/10.1021/prechem.5c00360
Precis. Chem. XXXX, XXX, XXX−XXX

surface after bubble departure directly determined the frequency of nucleation site activation and the rate of microlayer evaporation.[52,109−111] The pristine copper substrate exhibited an advancing contact angle (ACA) of 98° ± 4° and a receding contact angle (RCA) of approximately 76° ± 3°, characteristic of moderate hydrophobicity typical of clean metallic surfaces, as presented in Table S7 of SI. This moderate wettability, combined with relatively high contact angle hysteresis of approximately 22°, indicated significant contact line pinning and slower rewetting kinetics on the baseline substrate. Upon HEO deposition, all four compositions induced a transition toward enhanced hydrophilicity. The advancing contact angles decreased across the composition series, ranging from approximately 79° ± 3° for Y-HEO to 89° ± 5° for La-HEO. More significantly, the receding contact angles showed substantial reduction, dropping to 67° ± 6° for Y-HEO, 68° ± 4° for La-HEO, 62° ± 4° for Al-HEO, and 54° ± 2° for Mg-HEO. These reductions indicate that HEO deposition fundamentally improves liquid penetration into surface asperities, confirming Wenzel-state wetting, where the liquid fully wets surface roughness features rather than resting on air pockets.[112−114]

The contact angle hysteresis defined as the difference between advancing and receding angles and indicative of contact line pinning resistance emerged as a key discriminating metric across the compositions shown in Figure 5e. Y-HEO achieved notably low hysteresis of approximately 12° ± 7°, substantially lower than Al-HEO that reported 24° ± 6°, La-HEO at 21° ± 6°, and Mg-HEO at 27° ± 4°. This low hysteresis for Y-HEO is particularly significant because it represents an optimized balance between surface properties: the high roughness created by dense particle deposition of around Ra ≈ 0.63 μm provided abundant nucleation cavities and pinning sites,[115−117] while the low hysteresis indicated that the contact line can depin and repin readily, enabling rapid liquid rewetting without excessive stick−slip behavior.[118−120] The low-hysteresis and high-roughness combination indicates the facilitation of bubble departure on Y-HEO-modified surfaces through reduced contact line resistance while simultaneously providing stable nucleation cavities through moderate pinning.[121−123] In contrast, higher hysteresis values of Mg-HEO, 27° ± 4°, indicated stronger contact line pinning that, while potentially deepening cavities, also impedes the rapid rewetting cycle essential for maintaining a high nucleation frequency. The trade-off between these competing effects—cavity retention versus rewetting speed—appeared optimized for Y-HEO, explaining its superior performance in both CHF at 2017 ± 55 kW/m^2 and HTC of 123 ± 3 kW/m^2·°C.

Energy-dispersive X-ray spectroscopy mapping of the Y-HEO-deposited surface, shown in Figure 5f, provides direct confirmation that the multielement oxide particles successfully adhered to the copper substrate and retained compositional complexity throughout the boiling process. Individual elemental maps reveal the spatial distribution of all five constituent cations: yttrium (Y, red channel), cobalt (Co, green channel), chromium (Cr, blue channel), iron (Fe, cyan channel), manganese (Mn, magenta channel), and nickel (Ni, yellow). The elemental signals show a relatively uniform distribution across the substrate, with minor local fluctuations that correspond to particle density variations visible in the accompanying SEM image. This homogeneous elemental distribution demonstrates that the deposited HEO layer maintains the stoichiometric complexity and multielement character of the original synthesized powder.[124−126] The absence of preferential enrichment or depletion of any single element indicates that no phase separation or selective dissolution occurred during the boiling process. Furthermore, the correlation between elemental distribution patterns and particle morphology in the SEM image confirms that entire HEO particles, rather than dissociated ion species or partially dissolved oxides, comprise the deposited layer. This particle-level compositional integrity is critical for the proposed multielement surface heterogeneity and its associated interfacial phenomena[124,127,128] remain operative throughout thermal cycling. The sustained coverage and chemical completeness of the Y-HEO layer contributed substantially to its superior and stable performance in both the CHF and HTC metrics.

The integrated analysis of surface roughness, contact angle hysteresis, and elemental composition revealed how fundamental materials chemistry principles, specifically compositional complexity in HEOs, govern interfacial properties at the boiling surface. Y-HEO's exceptional performance emerges from a synergistic combination of surface characteristics: First, the highest surface roughness of Ra = 0.63 μm, 174% above baseline, provided the highest density of potential nucleation sites, enabling bubble formation at lower superheat and generating higher nucleation site density. Second, the lowest contact angle hysteresis of 12° ± 7° among all tested compositions enables efficient bubble departure and rapid liquid replenishment, maximizing the frequency with which nucleation sites can be reactivated and minimizing the risk of nucleate boiling collapse from extended dry-out periods. Third, uniform elemental distribution across the deposited layer verified by EDS mapping ensured that the multielement surface chemistry remains operative throughout boiling, maintaining the proposed heterogeneous interfacial water structures and electrostatic stabilization mechanisms established for dispersed HEO particles. These three properties—roughness, rewetting efficiency, and compositional heterogeneity—collectively corroborate the superior performance of Y-HEO across all thermal metrics. The data established precision design of multielement oxide composition that directly determines interfacial properties at multiple length scales, from the atomic-scale multielement surface heterogeneity confirming compositional complexity is operative to the micrometer-scale roughness influencing bubble nucleation to the macroscopic thermal performance translating interfacial control into functional enhancement. This materials-chemistry-first perspective, where boiling performance serves as a sensitive probe of surface and interfacial properties, represents the central contribution of this investigation to understanding structure−property relationships in high-entropy materials.

4. DISCUSSION

The sustained dispersion of HEO particles throughout the pool boiling experiments reflected a combination of thermodynamic driving forces and kinetic transport phenomena that work synergistically to maintain the particle suspension. At the thermodynamic level, the configurational entropy of the HEO system provided a fundamental stabilization mechanism that was absent in conventional single or binary oxide systems. The configurational entropy values calculated for the studied HEOs range from 13.38 to 14.90 J/mol·K, exceeding the critical 1.5R threshold of approximately

https://doi.org/10.1021/prechem.5c00360
Precis. Chem. XXXX, XXX, XXX−XXX

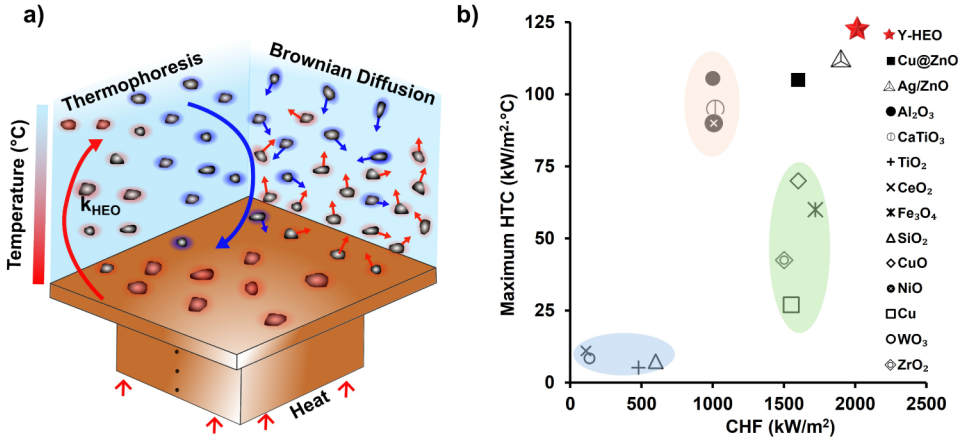

Figure 6. HEO particle transport and thermal performance positioning. (a) Schematic showing synergistic effects of Brownian diffusion (blue arrows) maintaining bulk dispersion and thermophoretic transport (red arrows) driving particle concentration toward the heated surface during pool boiling. (b) Performance benchmark showing Y-HEO positioned in the superior region (upper right), achieving both high CHF and high HTC, compared to conventional single-component oxides limited to either high CHF (green) or high HTC (orange), but not both. Literature data were included for the comparison of Y-HEO dispersion performance with literature-reported metal oxide additives: Cu@ZnO,[144] Ag/ZnO,[145] Al_2O_3,[146] $CaTiO_3$,[147] TiO_2,[148] CeO_2,[40] Fe_3O_4,[149] SiO_2,[150] CuO,[151] NiO,[147] Cu,[152] WO_3,[153] and ZrO_2.[154]

12.5 J/mol·K required for entropy-driven single-phase stabilization. This high entropy contributed substantially to the Gibbs free energy through the relationship:

$$\Delta G = \Delta H - T\Delta S \tag{3}$$

As temperature increased toward boiling conditions, the entropic term $T\Delta S$ dominated, providing growing thermodynamic resistance to particle aggregation. At elevated temperatures, this entropy-driven contribution became approximately 3.9 to 4.5 kJ/mol, substantially larger than the equivalent enthalpic penalties that would favor aggregation. Consequently, the dispersed state of randomly distributed HEO particles represented the thermodynamically favored configuration at boiling temperatures, providing inherent resistance to the sedimentation and agglomeration that typically threaten conventional colloidal dispersion stability. Complementing this thermodynamic stabilization, electrostatic interactions governed by classical DLVO theory provided kinetic barriers to particle aggregation.[129] The measured pH of 6.7 in HEO dispersions, compared to the calculated IEP near 8.0, indicated that oxide particle surfaces carried a positive charge. This electrostatic surface charge generated a Gouy−Chapman diffuse double layer that produced repulsive forces between similarly charged particles, opposing the VdW attraction that would otherwise drive aggregation.[130] Critically, the multielement composition of HEOs created surface heterogeneity that enhanced this electrostatic stabilization beyond what homogeneous oxides could achieve.[131] Different metal cations present on the HEO surface exhibited distinct pK_a values for hydroxyl group protonation, creating spatially varying surface charge distributions.[77] Rather than a single uniform IEP, the HEO surface exhibited a landscape of local charge variations that reduced the likelihood that all particles simultaneously reached neutral charge. This compositional complexity also enabled preferential adsorption of trace ions from the aqueous medium in composition-specific ways, further modulating the effective surface charge. The extended Debye length in low ionic strength DI water amplified these electrostatic interactions,[81−84] creating long-range repulsive forces effective at the micrometer-scale interparticle spacings characteristic of the studied HEO dispersions. Beyond simple electrostatic forces, the heterogeneous multielement surfaces of HEOs supported complex interfacial water structures that created additional stabilization through hydration forces.[91−97] Each transition metal cation in the HEO composition exhibited distinct water coordination preferences and Lewis acidity. Strong-field cations such as Cr^{3+} and Fe^{3+} coordinated water molecules more tightly than weaker cations, creating spatial variation in the hydration layer strength across the particle surface. This heterogeneous hydration landscape generated a spatially complex repulsive force distribution as particles approached one another, providing more effective stabilization than the uniform hydration forces expected from homogeneous oxide surfaces. Y-HEO dispersions remained visually stable for 48 h despite a 2.3 pH unit difference from the calculated IEP, suggesting that mechanisms beyond simple electrostatic repulsion operated, consistent with the proposed hydration force contributions.

The formation of the observed dense particle deposition layers on the copper substrates during boiling reflected the interplay between Brownian motion, thermophoresis, and surface interactions.[132−134] Figure 6a illustrates these competing transport mechanisms. Brownian motion, driven by thermal energy, imparts random molecular-scale displacements that maintain bulk mixing and prevent sedimentation.[98−100] For micrometer-scale particles, gravitational settling times span from seconds to tens of seconds, comparable to time scales governed by thermal diffusivity.[135] However, the convective mixing generated by bubble nucleation and growth in pool boiling overpowered gravitational effects, maintaining bulk dispersion regardless of particle size.[136] More significantly, steep temperature gradients near the heated copper surface create powerful thermophoretic forces that drive direct particle transport. In aqueous oxide dispersions, thermophoresis typically transports particles from cooler bulk regions toward the hot surface.[137,138] The Soret coefficient for metal oxide particles in water typically ranges from 10^{-3} to 10^{-2} K^{-1}, corresponding to particle velocities of millimeters per minute in the temperature gradients exceeding 10^6 K/m that develop near a boiling surface.[139,140] Over the 30-to-60-min duration of pool boiling experiments, such velocities readily transport particles from bulk liquid at room temperature to the heated

https://doi.org/10.1021/prechem.5c00360
Precis. Chem. XXXX, XXX, XXX−XXX

surface region at boiling temperature, creating sustained particle accumulation. The synergy between thermophoresis and colloidal stability becomes apparent: electrostatic[141] and entropic forces[142] maintain dispersion in the bulk liquid, preventing premature aggregation, while thermophoretic forces concentrate particles at the surface where their deposition creates the observed surface modifications.[143] This combination enabled the 0.05 wt % concentration to achieve optimal performance, representing the balance point where sufficient particle flux reaches the surface to dramatically modify its properties while the bulk concentration remains diluted enough to avoid viscosity penalties or rapid settling.

The composition-dependent variations in surface roughness, wettability, and elemental distribution directly explain the corresponding variations in thermal performance across the four HEO compositions. Scanning electron microscopy revealed that Y-HEO created the most pronounced surface modification, with arithmetic average roughness increasing 174% from the baseline polished copper value of 0.23 ± 0.06 μm to 0.63 ± 0.08 μm. Other compositions produced intermediate roughness values ranging from 0.33 to 0.57 μm. Energy-dispersive X-ray spectroscopy mapping confirmed that the Y-HEO surface retained all five constituent cations in a uniform spatial distribution, validating that the complex multielement oxide character persists in the deposited layer. This increased roughness creates abundant nucleation cavities for vapor bubble formation. The Clausius−Clapeyron equation, combined with Young−Laplace analysis, demonstrates that the reduced wall superheat is associated with smaller bubble nucleation cavities. The relationship shows an inverse proportionality between wall superheat and cavity radius:

$$\Delta T_{ws} = \frac{2\sigma T_{sat} \upsilon_{lv}}{r h_{fg}} \tag{4}$$

Here, σ is surface tension, υ_{lv} is specific volume between the liquid and vapor phase, r is the radius of curvature of the bubble or cavity radius, and h_{fg} is the heat of vaporization. Larger cavities reduce the superheat required for bubble nucleation, enabling more nucleation sites to activate simultaneously and increasing overall nucleation frequency. The observed 8 °C reduction in wall superheat for Y-HEO compared to the baseline reflects this phenomenon. Empirical correlations from the literature indicate that CHF scales with the square root of surface roughness,[155] and HTC increases exponentially with roughness[156] due to enhanced nucleation activity and improved liquid replenishment.[157−160] However, surface roughness alone does not explain Y-HEO's superior performance. DCA analysis reveals that the low contact angle hysteresis of Y-HEO, 12 ± 7°, distinguishes it from other compositions, 21 to 27°, despite all showing enhanced wettability compared to the baseline. Contact angle hysteresis characterizes the resistance to contact line motion and governs how readily the liquid wets and rewets the surface after bubble departure. Low hysteresis indicates that advancing and receding contact lines can readily repin and depin, enabling rapid liquid replenishment to the nucleation sites after bubble departure. This efficient rewetting allows nucleation sites to reactivate quickly, maximizing the frequency of bubble generation and minimizing the risk of nucleate boiling collapse from extended dry periods.[38,161,162] The combination of high roughness providing nucleation cavities and low hysteresis enabling efficient rewetting appears optimized for Y-HEO, explaining its achievement of both the highest CHF of 2017 ± 55 kW/m^2 and the highest HTC of 123 ± 3 kW/m^2·°C. The composition-dependent differences in deposition quality reflect fundamental differences in how elemental composition influences particle adhesion and packing behavior.[163,164] Y-HEO features yttrium as the primary A-site cation in a perovskite structure, while Al-HEO adopts a spinel geometry and Mg-HEO a rock-salt structure. Yttrium's high charge density and specific ionic radius likely enhance interaction with the copper substrate, promoting stronger particle adhesion and denser packing.[165] Furthermore, yttrium's hydrophilic character and distinctive water coordination preferences may promote preferential particle orientation during deposition, creating optimal configurations for nucleation site functionality.[166] The connection among surface roughness, nucleation site density, and required superheat can be further interpreted using the cavity nucleation framework that has been applied to structured surfaces. Prior work on reduced graphene oxide coatings and microcavity arrays has shown that maximum enhancement is obtained when surface features create cavities whose radii fall within the micrometer range favored by the local thermodynamic conditions. The analysis based on eq 4 indicates that the Y-HEO-modified surface produces effective cavity sizes in this same range, consistent with the observed SEM topography. In contrast to top-down-fabricated microstructures, the HEO coatings achieve this favorable distribution of nucleation sites through self-organized particle deposition during boiling. This suggests that colloidal deposition of high-entropy oxides can provide a practical route to generating effective nucleation cavities similar to those realized in engineered micro- and nanostructured surfaces, while simultaneously tuning wettability and contact angle hysteresis.

Figure 6b contextualizes the Y-HEO performance within the broader landscape of metal oxide pool boiling additives reported in the literature. Conventional additives fall into three categories: compositions achieving high CHF but low HTC, leaving large wall temperature differences (light green region); compositions providing high HTC but limited CHF with premature dry-out risk (light orange region); and inefficient compositions performing poorly in both metrics (light blue region). Examples spanning these categories include CuO, ZrO_2, and Fe_3O_4 yielding high CHF, low HTC; Al_2O_3, $CaTiO_3$, and NiO producing high HTC but limited CHF; and SiO_2, TiO_2, WO_3, and CeO_2 resulting in poor overall performance. In contrast, the HEO compositions investigated in this work achieve both high CHF and high HTC, positioning them distinctly above the performance envelope of conventional single-component oxides. Y-HEO achieved a CHF of ∼2017 kW/m^2 and HTC of ∼123 kW/m^2·°C, surpassing the performance achieved by Cu@ZnO and Ag/ZnO, previously reported as the most effective metal oxide systems for pool boiling. This superior performance gained importance when combined with economic and practical considerations. Cu@ZnO was investigated on copper microchannels rather than flat surfaces, limiting direct comparison to relevant applications. Ag/ZnO, while achieving high performance, incorporates expensive metallic silver, whereas Y-HEO derives from abundant, inexpensive elements. This combination of superior performance, compatibility with conventional test geometries, and economic feasibility positions HEOs as

https://doi.org/10.1021/prechem.5c00360
Precis. Chem. XXXX, XXX, XXX−XXX

the most promising metal oxide additives for pool boiling thermal management applications.

The exceptional thermal performance of Y-HEO emerged from a synergistic combination of mechanisms operating across multiple length scales, each rooted in fundamental materials chemistry principles. The high configurational entropy of the multielement oxide composition enables thermodynamically favored dispersion at elevated temperatures.[167−170] The heterogeneous multielement surface chemistry generates enhanced electrostatic stabilization and complex interfacial water structures not achievable in conventional oxides. The composition-optimized particle adhesion and packing behavior produce superior surface roughness and nucleation site density. The distinctive interfacial chemistry of the Y-containing composition creates optimally low contact angle hysteresis, balancing nucleation site retention with efficient rewetting. These mechanisms do not operate independently but rather synergistically. Simultaneously, thermophoretic forces concentrate particles at the heated surface. The multielement composition optimizes both the dispersed stability and the interfacial functionality, accomplishing goals that would involve irreconcilable trade-offs for single-component oxides. This synergy represents the central advantage of the high-entropy approach: compositional complexity provides flexibility to optimize multiple competing properties simultaneously rather than selecting one element that performs reasonably across all requirements. The framework connecting HEO composition through colloidal stability to thermal performance establishes that precision chemistry approaches to material synthesis directly translate into functional advantages in demanding applications. The eight HEO compositions explored, spanning three distinct crystal structures, all exceeded the thermal performance of conventional oxide additives, suggesting that the high-entropy principle itself confers stabilization and functional benefits transcending specific structural choices. However, Y-HEO's superior performance compared to other perovskite compositions indicates that specific elemental composition critically influences the functional response. Future systematic variation of HEO composition while maintaining a fixed crystal structure would illuminate which elemental substitutions most strongly enhance thermal performance and reveal the underlying mechanistic basis for these composition−performance correlations.

However, several limitations constrain the mechanistic conclusions drawn from the current work. The absence of in situ characterization during active boiling prevents direct observation of whether the proposed mechanisms actually operate under thermal cycling conditions. Time-resolved small-angle X-ray scattering during heating would directly monitor particle aggregation state transitions. Neutron reflectometry with temperature variation would image interfacial water structure changes. High-speed video microscopy during boiling would directly visualize bubble dynamics, contact line behavior, and nucleation site activation sequences. These advanced techniques would either validate or refute the proposed mechanism by providing direct evidence unavailable through postboiling surface analysis. The 48-h room temperature stability assessment provides evidence of near-term dispersion robustness but cannot predict long-term performance under extended thermal cycling conditions relevant to real applications. In addition, the present surface characterization captures only the final state after the completion of a full boiling sequence. The copper substrates experience a cumulative history of increasing heat flux during each experiment, and the resulting HEO deposition reflects the integrated action of thermophoretic transport and hydrodynamic removal over that sequence. The current study does not resolve how surface roughness and deposition morphology evolve with time at fixed heat flux or how different dwell times at a given flux might modify the balance between particle accumulation and removal. Dedicated experiments in which boiling is conducted at a single, controlled heat flux for systematically varied durations would be valuable to quantify deposition kinetics and to decouple time-dependent effects from the cumulative history considered here. A further limitation of this study is the absence of direct visualization of bubble dynamics during boiling. The current apparatus does not provide optical access for high-speed imaging; therefore, the influence of HEO deposition on nucleation site activation, bubble growth, coalescence, and departure must be inferred from surface measurements and boiling curves rather than observed directly. Future work should incorporate transparent heater substrates or side-viewing windows together with high-speed cameras to quantify the bubble departure diameter, nucleation site density, and local rewetting behavior for each HEO composition across a range of heat fluxes. Such measurements would provide an important link between the surface modifications documented here and the detailed two-phase flow structures that ultimately control the boiling heat transfer.

The dilute nature of HEO dispersions at 0.05 wt % concentration ensures that bulk thermophysical properties contribute minimally to the observed thermal performance enhancements. At this concentration, the particle volume fraction is approximately 0.015 to 0.020 vol %, well below thresholds where significant property modifications occur. Literature data compiled in Table S6 demonstrate that viscosity, surface tension, and thermal conductivity changes at 0.05 wt % are typically within 1 to 3% of the base fluid values. Our recently published work on rheological characterization of $Ti_3C_2T_x$ MXene dispersions at 0.1 wt %, double the concentration used in this study, showed viscosity increases of only 1.4%, well within experimental error. Extensive studies on dilute metal oxide nanofluids have reported similar trends: Sundar et al. measured Fe_3O_4−water nanofluids at 0, 0.2, and 0.4 vol % and found negligible viscosity deviations from water across temperatures from 20 to 60 °C.[171] ZnO−water dispersions were characterized, and it was observed that surface tension remained within 2% of that of water at 0.05 wt %, increasing slightly before decreasing at higher concentrations.[172]

Classical pool boiling heat transfer correlations provide a quantitative assessment of the expected influence of these minor property changes. The Rohsenow correlation[173] for the nucleate boiling heat transfer coefficient can be expressed as:

$$\frac{c_p \Delta T_{WS}}{h_{fg}} = C_{sf}\left[\frac{q''}{\mu_l h_{fg}}\sqrt{\frac{\sigma}{g(\rho_l - \rho_v)}}\right]^{0.33}\left(\frac{c_p \mu}{k}\right)^n \quad (5)$$

where μ_l is dynamic viscosity, σ is surface tension, and the other parameters represent fluid properties and empirical constants. For the measured property variations at 0.05 wt % + 2% viscosity, −2% surface tension, negligible density, and specific heat changes reported, this correlation predicts less

https://doi.org/10.1021/prechem.5c00360
Precis. Chem. XXXX, XXX, XXX−XXX

than 3% variation in heat flux at constant superheat. Similarly, the Zuber correlation[174] for critical heat flux:

$$q''_{CHF} = K \times h_{fg}\rho_g^{1/2}\left[\sigma g(\rho_l - \rho_g)\right]^{1/4} \quad (6)$$

predicts that the −2% surface tension change would produce less than 0.5% CHF reduction, far below measurement uncertainty. In contrast, experimental measurements reveal CHF enhancements ranging from 62% for Al-HEO to 95% for La-HEO, and HTC improvements ranging from 85% for Al-HEO to 135% for Y-HEO. These performance gains are more than an order of magnitude larger than bulk property modifications alone could produce. This quantitative discrepancy confirms the central hypothesis of this work: that HEO-enhanced pool boiling operates primarily through surface modification and interfacial chemistry mechanisms rather than through altered bulk fluid properties. Enhanced roughness of 174% increase for Y-HEO dramatically reduces contact angle from 96° to 62°, minimizes hysteresis (12° versus 22° baseline), and directly modifies nucleation site density, bubble departure frequency, and liquid rewetting efficiency at the heated surface. These interfacial phenomena govern thermal transport in nucleate boiling far more strongly than minor variations in bulk viscosity or surface tension. The multielement surface composition creates chemical heterogeneity at the solid−liquid interface that generates advantageous wetting characteristics and nucleation behavior unavailable through simple bulk property modification alone. This further corroborates that performance optimization should focus on engineering interfacial properties through precise control of particle deposition, surface chemistry, and wettability modification rather than pursuing high particle loadings that increase viscosity and pumping power without commensurate thermal benefits.

Future work will involve characterizing dispersion stability over weeks to months at elevated temperatures with periodic characterization tracking of sedimentation, aggregation, and chemical stability. Extended thermal cycling would reveal whether the proposed entropy-driven stabilization maintains effectiveness under repeated temperature fluctuations and whether any irreversible oxidation or surface chemistry changes occur. Contact angle and roughness measurements characterize only the final postboiling surface state. Dynamic contact line behavior during active boiling, the temporal evolution of roughness as particles accumulate, and the transient bubble dynamics driving nucleation remain unmeasured. High-speed microscopy and in situ surface characterization techniques would directly observe these dynamic phenomena and quantify bubble departure frequencies, nucleation site activation sequences, and rewetting rates. Despite these limitations, the current investigation establishes that compositional complexity in multielement oxides represents a productive strategy for simultaneously optimizing multiple properties essential for demanding thermal applications. Additionally, systematically varying composition while maintaining crystal structure is warranted to illuminate which elemental substitutions most strongly enhance performance, establishing the quantitative structure−property correlations that precision chemistry seeks to develop and enabling the rational design of next-generation high-entropy materials for thermal management and related applications.

5. CONCLUSIONS

This work demonstrated that precision chemistry principles governing high-entropy oxide synthesis and compositional design directly translate into advantageous colloidal and interfacial behavior, manifested in exceptional functional performance under thermal stress. The fundamental finding that HEOs with five or more equimolar cations exhibited enhanced dispersion stability compared to lower-entropy oxide systems provided direct experimental evidence for configurational entropy contributions to colloidal thermodynamics. The configurational entropy values of 13.38 to 14.90 J/mol·K, exceeding the critical 1.5R threshold, generated substantial thermodynamic driving force against particle aggregation, particularly at elevated temperatures where the $T\Delta S$ term dominates the Gibbs free energy. The random distribution of multiple metal cations across HEO particle surfaces created chemical heterogeneity that generated superior interfacial chemistry through multiple complementary mechanisms, including electrostatic stabilization via spatially varying surface charge, hydration force enhancement from diverse metal−water coordination environments, and interfacial water structuring arising from compositional complexity. The Y-HEO system demonstrated exceptional functional performance in pool boiling experiments, achieving 63% CHF enhancement and 135% HTC improvement compared to baseline deionized water. This exceptional performance emerged from the synergistic interplay of multiple thermodynamic and kinetic factors: multielement surface composition generates optimized wettability characteristics that produce abundant nucleation sites, configurational entropy provides thermodynamic stabilization that maintains particle dispersion; and thermophoretic transport concentrates particles at the heated surface, enabling effective surface modification. The combination yielded the highest surface roughness, representing a 174% increase, lowest contact angle hysteresis at ∼12°, and most uniform elemental distribution among tested compositions, directly correlating with superior thermal performance. This work establishes that thermal applications provide a valuable platform for understanding structure−function relationships in high-entropy materials, where pool boiling creates an extreme environment, simultaneously testing colloidal stability under thermal gradients and interfacial chemistry under active nucleation and phase change. The compositional flexibility of high-entropy materials enables simultaneous optimization of multiple competing properties, overcoming fundamental trade-offs that constrain single-component or binary oxide systems. The Y-HEO system achieved thermal performance exceeding all literature-reported single-component oxide systems and matching or surpassing hybrid systems such as Cu@ZnO and Ag/ZnO while incorporating abundant, inexpensive elements, positioning HEOs as the most promising metal oxide additives for pool boiling thermal management applications. Future work will emphasize the systematic variation of HEO composition while maintaining fixed crystal structure to isolate entropy effects from structural contributions and establish quantitative structure−property correlations. Advanced characterization, including surface-specific spectroscopy, atomic force microscopy, force spectroscopy, and high-speed video microscopy, is warranted to observe interfacial phenomena and provide experimental evidence for proposed mechanisms of entropy-driven stabilization. Furthermore, investigation of nonequimolar high-entropy compo-

https://doi.org/10.1021/prechem.5c00360
Precis. Chem. XXXX, XXX, XXX−XXX

sitions would expand the compositional design space, while extension to other thermal applications and heterogeneous catalysis would test the generality of findings.

■ ASSOCIATED CONTENT

Data Availability Statement

Raw data are available upon request.

Supporting Information

The Supporting Information is available free of charge at https://pubs.acs.org/doi/10.1021/prechem.5c00360.

S1: Initial screening: composition-dependent colloidal stability and selection criteria for pool boiling candidates; S2: Pool boiling experimental apparatus and heat flux determination methodology; S3: Thermal conductivity calculation for high-entropy oxide compositions; S4: Particle size distribution analysis via digital image microscopy; S5: Isoelectric point estimation from constituent oxide literature values; S6: Thermal performance of nonselected HEO compositions and concentration optimization study; S7: Error budget and uncertainty propagation for thermal measurements; S8: Postboiling surface characterization: roughness and topography analysis via optical microscopy; S9: Concentration optimization study (PDF)

■ AUTHOR INFORMATION

Corresponding Author

Anju Gupta − *Department of Mechanical, Industrial and Manufacturing Engineering, The University of Toledo, Toledo, Ohio 43606, United States;* orcid.org/0000-0001-5378-9496; Phone: +1-(413)-530-8213; Email: anju.gupta@utoledo.edu

Authors

Keval Bharatbhai Suthar − *Department of Mechanical, Industrial and Manufacturing Engineering, The University of Toledo, Toledo, Ohio 43606, United States*

Manjula M. Kandage − *Department of Chemistry and Biochemistry, The University of Toledo, Toledo, Ohio 43606, United States*

Md Moynul Hasan − *Department of Mechanical, Industrial and Manufacturing Engineering, The University of Toledo, Toledo, Ohio 43606, United States*

Saketh Merugu − *Department of Mechanical, Industrial and Manufacturing Engineering, The University of Toledo, Toledo, Ohio 43606, United States*

Michal Marszewski − *Department of Chemistry and Biochemistry, The University of Toledo, Toledo, Ohio 43606, United States;* orcid.org/0000-0002-4157-3046

Complete contact information is available at: https://pubs.acs.org/10.1021/prechem.5c00360

Author Contributions

K.B.S.: Investigation, visualization, data curation, formal analysis, and writing—original draft; M.M.K.: Methodology and investigations; M.M.H.: Investigation; S.M.: Methodology, investigation, visualization, writing—review and editing; M.M.: Methodology, supervision, and writing—review and editing; A.G.: Conceptualization, project administration, supervision, and writing—review and editing.

Notes

The authors declare that all funding sources have been fully disclosed and that there are no additional financial or nonfinancial conflicts of interest related to this work.
The authors declare no competing financial interest.

■ ACKNOWLEDGMENTS

This research was supported in part by startup funds provided to Dr. Michal Marszewski by the University of Toledo.

■ REFERENCES

(1) Brahlek, M.; Gazda, M.; Keppens, V.; Mazza, A. R.; McCormack, S. J.; Mielewczyk-Gryń, A.; Musico, B.; Page, K.; Rost, C. M.; Sinnott, S. B.; et al. What is in a name: Defining "high entropy" oxides. *APL Mater.* **2022**, *10* (11), 110902.

(2) Musicó, B. L.; Gilbert, D.; Ward, T. Z.; Page, K.; George, E.; Yan, J.; Mandrus, D.; Keppens, V. The emergent field of high entropy oxides: Design, prospects, challenges, and opportunities for tailoring material properties. *APL Mater.* **2020**, *8* (4), 040912.

(3) Yang, Z.; Xiang, X.; Yang, J.; Zhao, Z.-Y. High-entropy oxides as energy materials: from complexity to rational design. *Mater. Futures* **2024**, *3* (4), 042103.

(4) Khoroshun, K.; González-Rivas, M. U.; Hallas, A. M. More Is Different: Case Studies of How Chemical Complexity Influences Stability in High Entropy Oxides. *Chem. Mater.* **2025**, *37*, 9524−9532.

(5) Rost, C. M.; Mazza, A. R.; McCormack, S. J.; Page, K.; Sarkar, A.; Ward, T. Z. Era of entropy: Synthesis, structure, properties, and applications of high-entropy materials. *Appl. Phys. Lett.* **2024**, *125* (20), 200401.

(6) Dey, G. R.; Soliman, S. S.; McCormick, C. R.; Wood, C. H.; Katzbaer, R. R.; Schaak, R. E. Colloidal nanoparticles of high entropy materials: Capabilities, challenges, and opportunities in synthesis and characterization. *ACS Nanosci. Au* **2024**, *4* (1), 3−20.

(7) Chen, D.; Zhu, X.; Yang, X.; Yan, N.; Cui, Y.; Lei, X.; Liu, L.; Khaliq, J.; Li, C. A review on structure−property relationships in dielectric ceramics using high-entropy compositional strategies. *J. Am. Ceram. Soc.* **2023**, *106* (11), 6602−6616.

(8) Yao, Y.; Dong, Q.; Brozena, A.; Luo, J.; Miao, J.; Chi, M.; Wang, C.; Kevrekidis, I. G.; Ren, Z. J.; Greeley, J.; et al. High-entropy nanoparticles: Synthesis-structure-property relationships and data-driven discovery. *Science* **2022**, *376* (6589), abn3103.

(9) Yen, J.-Z.; Yang, Y.-C.; Tuan, H.-Y. Interface engineering of high entropy Oxide@ Polyaniline heterojunction enables highly stable and excellent lithium ion storage performance. *Chem. Eng. J.* **2022**, *450*, 137924.

(10) Bao, W.; Shen, H.; Zhang, Y.; Qian, C.; Zeng, G.; Jing, K.; Cui, D.; Xia, J.; Liu, H.; Guo, C.; et al. High-entropy oxides for energy storage and conversion. *J. Mater. Chem. A* **2024**, *12* (35), 23179−23201.

(11) Xing, J.; Liu, Y.; Mathew, G.; He, Q.; Aghassi-Hagmann, J.; Schweidler, S.; Breitung, B. High-Entropy Metal−Organic Frameworks and Their Derivatives: Advances in Design, Synthesis, and Applications for Catalysis and Energy Storage. *Adv. Sci.* **2025**, *12* (5), 2411175.

(12) Wang, Y.; Mi, J.; Wu, Z.-S. Recent status and challenging perspective of high entropy oxides for chemical catalysis. *Chem. Catal.* **2022**, *2* (7), 1624−1656.

(13) Li, X.; Zou, Y.; Lu, H.; Wang, L. Nanoscale high-entropy alloys for solar and thermal applications. *Nanoscale* **2025**, *17*, 6266−6286.

(14) Aamlid, S. S.; Oudah, M.; Rottler, J.; Hallas, A. M. Understanding the role of entropy in high entropy oxides. *J. Am. Chem. Soc.* **2023**, *145* (11), 5991−6006.

(15) Anand, G.; Wynn, A. P.; Handley, C. M.; Freeman, C. L. Phase stability and distortion in high-entropy oxides. *Acta Mater.* **2018**, *146*, 119−125.

(16) Fracchia, M.; Coduri, M.; Ghigna, P.; Anselmi-Tamburini, U. Phase stability of high entropy oxides: A critical review. *J. Eur. Ceram. Soc.* **2024**, *44* (2), 585−594.
(17) Riley, C.; De La Riva, A.; Park, J. E.; Percival, S. J.; Benavidez, A.; Coker, E. N.; Aidun, R. E.; Paisley, E. A.; Datye, A.; Chou, S. S. A high entropy oxide designed to catalyze CO oxidation without precious metals. *ACS Appl. Mater. Interfaces* **2021**, *13* (7), 8120−8128.
(18) Sarkar, A.; Wang, Q.; Schiele, A.; Chellali, M. R.; Bhattacharya, S. S.; Wang, D.; Brezesinski, T.; Hahn, H.; Velasco, L.; Breitung, B. High-entropy oxides: fundamental aspects and electrochemical properties. *Adv. Mater.* **2019**, *31* (26), 1806236.
(19) Su, L.; Huyan, H.; Sarkar, A.; Gao, W.; Yan, X.; Addiego, C.; Kruk, R.; Hahn, H.; Pan, X. Direct observation of elemental fluctuation and oxygen octahedral distortion-dependent charge distribution in high entropy oxides. *Nat. Commun.* **2022**, *13* (1), 2358.
(20) Kotsonis, G. N.; Almishal, S. S.; Marques dos Santos Vieira, F.; Crespi, V. H.; Dabo, I.; Rost, C. M.; Maria, J. P. High-entropy oxides: Harnessing crystalline disorder for emergent functionality. *J. Am. Ceram. Soc.* **2023**, *106* (10), 5587−5611.
(21) Wang, J.; Sun, S.; Xi, S.; Sun, Y.; Ong, S. J. H.; Seh, Z. W.; Xu, Z. J. High-entropy spinel oxides for water oxidation: surface entropy evolution and activity promotion. *J. Phys. Chem. C* **2024**, *128* (12), 4978−4987.
(22) Sen, S.; Palabathuni, M.; Ryan, K. M.; Singh, S. High Entropy Oxides: Mapping the Landscape from Fundamentals to Future Vistas: Focus Review. *ACS Energy Lett.* **2024**, *9* (8), 3694−3718.
(23) Segets, D.; Marczak, R.; Schäfer, S.; Paula, C.; Gnichwitz, J.-F.; Hirsch, A.; Peukert, W. Experimental and theoretical studies of the colloidal stability of nanoparticles− a general interpretation based on stability maps. *ACS Nano* **2011**, *5* (6), 4658−4669.
(24) Chen, S.; Petersen, N.; Valsson, O.; Girard, M.; Wang, H. I. Understanding and Controlling the Colloidal Stability of CdSe Nanoplatelets by Solvation Force Engineering. *J. Am. Chem. Soc.* **2025**, *147* (39), 35347−35354.
(25) Chopada, R.; Sarwate, R.; Kumar, V. Effect of mild to extreme pH, temperature, and ionic strength on the colloidal stability of differentially capped gold nanoparticles. *J. Mol. Struct.* **2025**, *1323*, 140751.
(26) dos Santos, C. C.; Viali, W.; Viali, E.; Marques, R.; Jafelicci Junior, M. Colloidal stability study of Fe_3O_4-based nanofluids in water and ethylene glycol. *J. Therm. Anal. Calorim.* **2021**, *146*, 509−520.
(27) Jin, C.; Wu, Q.; Yang, G.; Zhang, H.; Zhong, Y. Investigation on hybrid nanofluids based on carbon nanotubes filled with metal nanoparticles: Stability, thermal conductivity, and viscosity. *Powder Technol.* **2021**, *389*, 1−10.
(28) Shah, J.; Ranjan, M.; Thareja, P.; Estellé, P. Tailoring stability and thermophysical properties of CuO nanofluid through ultra-sonication. *J. Therm. Anal. Calorim.* **2022**, *147* (19), 10319−10328.
(29) Wen, T.; Luo, J.; Jiao, K.; Lu, L. Experimental study on the pool boiling performance of a highly self-dispersion TiO_2 nanofluid on copper surface. *Int. J. Therm. Sci.* **2023**, *184*, 107999.
(30) Kangude, P.; Srivastava, A. On the mechanisms leading to ordered nanoparticles deposition during single bubble nucleate pool boiling regime. *Phys. Fluids* **2021**, *33* (11), 113306.
(31) Bhatt, D.; Kangude, P.; Srivastava, A. Simultaneous mapping of single bubble dynamics and heat transfer rates for SiO_2/water nanofluids under nucleate pool boiling regime. *Phys. Fluids* **2019**, *31* (1), 017102.
(32) Feroskhan, M.; Venugopal, T.; Almakayeel, N. M.; Khan, T. Y.; Khadar, S. D. A.; Gobinath, N. Effect of Thermophoresis on Heat Diffusion in Isobutane/Copper-Oxide Nanofluid under Pool Boiling Condition: Numerical Investigation. *J. Nanomater.* **2022**, *2022* (1), 2216513.
(33) Merugu, S.; Hasan, M. M.; Thakur, A.; Patenaude, J.; Anasori, B.; Choueiri, G.; Gupta, A. $Ti_3C_2T_x$ MXene Additives for Enhanced Pool Boiling Regime. *ACS Omega* **2025**, *10* (7), 6534−6543.
(34) Jiang, H.; Liu, Y.; Chu, H. A review of numerical investigation on pool boiling. *J. Therm. Anal. Calorim.* **2023**, *148* (17), 8697−8745.
(35) Marie, A.; Cioulachtjian, S.; Lips, S.; Sartre, V. Thermal interactions between nucleation sites and the solid wall during pool boiling of a pure fluid: A review. *Int. J. Therm. Sci.* **2022**, *174*, 107388.
(36) Kim, D. E.; Oh, J. S. Local phase and thermal behaviors in pool boiling on different wettability surfaces. *Exp. Therm. Fluid Sci.* **2022**, *139*, 110728.
(37) Hu, Z.; Yin, X.; Zhang, L.; Liang, G. Pool boiling on hybrid-wettability surfaces with phase-change lattice Boltzmann model. *Appl. Therm. Eng.* **2025**, *261*, 125101.
(38) Wei, J.; Liu, Z.; Gong, S.; Cheng, P. Effects of contact angle hysteresis on nucleate boiling bubble dynamics and heat transfer. *Int. J. Heat Mass Transfer* **2026**, *256*, 128122.
(39) Li, Y.; Li, Y.; Jiao, W.; Chen, X.; Lu, G. Manipulating the heat transfer of pool boiling by tuning the bubble dynamics with mixed wettability surfaces. *Int. J. Heat Mass Transfer* **2021**, *170*, 120996.
(40) Kamel, M. S.; Lezsovits, F. Enhancement of pool boiling heat transfer performance using dilute cerium oxide/water nanofluid: An experimental investigation. *Int. Commun. Heat Mass Transfer* **2020**, *114*, 104587.
(41) Peng, C.; Song, Y. Y.; Deng, J.; Wu, J.; Chen, H. L.; Liu, F. The influence of suspension and deposition on pool boiling heat transfer of nanofluids: Experiment and engineering model study. *Int. J. Heat Mass Transfer* **2024**, *227*, 125614.
(42) Park, H.; Nam, H. T.; Shin, S.; Lee, N.; Cho, H. H.; Lee, D. Enhancing pool boiling heat transfer performance via deposition of nanoparticles with different sizes on micropillar surfaces. *Int. Commun. Heat Mass Transfer* **2025**, *160*, 108282.
(43) Srinivas, T.; Adarsh Varma, P.; Satya Priya, C.; Prashanth, M.; Mukesh, P.; Sai Sri Nandan, B.; Srinivas, G. The effects of nanoparticles on pool boiling and critical heat flux. *Indian J. Phys.* **2025**, *99* (4), 1509−1518.
(44) Gupta, S. K.; Misra, R. D. Effect of Novel Cu@ZnO Hybrid Nanofluids on Pool Boiling Heat Transfer Performance. *Int. J. Thermophys.* **2023**, *44* (9), 134.
(45) Yasmin, H.; Giwa, S. O.; Noor, S.; Sharifpur, M. Thermal Conductivity Enhancement of Metal Oxide Nanofluids: A Critical Review. *Nanomaterials* **2023**, *13* (3), 597.
(46) Sundar, L. S.; Ramana, E. V.; Graça, M. P. F.; Singh, M. K.; Sousa, A. C. M. Nanodiamond-Fe3O4 nanofluids: Preparation and measurement of viscosity, electrical and thermal conductivities. *Int. Commun. Heat Mass Transfer* **2016**, *73*, 62−74.
(47) Nabil, M. F.; Azmi, W. H.; Hamid, K. A.; Mamat, R.; Hagos, F. Y. An experimental study on the thermal conductivity and dynamic viscosity of TiO2-SiO2 nanofluids in water: Ethylene glycol mixture. *Int. Commun. Heat Mass Transfer* **2017**, *86*, 181−189.
(48) Guo, Y.; Zhang, T.; Zhang, D.; Wang, Q. Experimental investigation of thermal and electrical conductivity of silicon oxide nanofluids in ethylene glycol/water mixture. *Int. J. Heat Mass Transfer* **2018**, *117*, 280−286.
(49) Abdolbaqi, M. K.; Azmi, W. H.; Mamat, R.; Sharma, K. V.; Najafi, G. Experimental investigation of thermal conductivity and electrical conductivity of BioGlycol-water mixture based Al_2O_3 nanofluid. *Appl. Therm. Eng.* **2016**, *102*, 932−941.
(50) Wang, C.-Y.; Ji, W.-T.; Zhao, C.-Y.; Chen, L.; Tao, W.-Q. Experimental determination of the role of roughness and wettability on pool-boiling heat transfer of refrigerant. *Int. J. Refrig.* **2023**, *153*, 205−221.
(51) Kangude, P.; Srivastava, A. Experiments to understand bubble base evaporation mechanisms and heat transfer on nano-coated surfaces of varying wettability under nucleate pool boiling regime. *Int. J. Multiphase Flow* **2022**, *152*, 104098.
(52) Allred, T. P.; Weibel, J. A.; Garimella, S. V. The effect of dynamic wetting behavior on boiling heat transfer mechanisms during bubble growth and departure. *Int. J. Heat Mass Transfer* **2022**, *184*, 122276.
(53) Mahmoud, M. M.; Karayiannis, T. G. Pool boiling review: Part I-Fundamentals of boiling and relation to surface design. *Therm. Sci. Eng. Prog.* **2021**, *25*, 101024.

https://doi.org/10.1021/prechem.5c00360
Precis. Chem. XXXX, XXX, XXX−XXX

(54) Li, J.; Zhao, Y.; Ma, J.; Fu, W.; Yan, X.; Rabbi, K. F.; Miljkovic, N. Superior antidegeneration hierarchical nanoengineered wicking surfaces for boiling enhancement. *Adv. Funct. Mater.* **2022**, *32* (8), 2108836.
(55) Sadaghiani, A.; Ozbey, A.; Karimzadehkhouei, M.; Koşar, A. Heat and fluid flow mechanisms and characterization. In *Nanofluid Boiling*. Ali Sadaghiani, A. O.; Karimzadehkhouei, MEHRDAD.; Koşar, A. L. I., eds.; Academic Press, pp. 73−125, 2024
(56) Chen, H.; Zhai, Y.; Bai, Y.; Chen, H.; Li, Z. Bubble behavior and heat transfer mechanisms of deposited nanoparticles in pool-boiling process. *Int. J. Therm. Sci.* **2025**, *218*, 110151.
(57) Krishnan, A.; Dhir, V. K. Numerical study of influence of lateral bubble merger on bubble dynamics and heat transfer during nucleate pool boiling on a horizontal substrate under a constant imposed heat flux. *Int. J. Heat Mass Transfer* **2025**, *247*, 127063.
(58) Kandage, M. M.; Marszewski, M. On the synthesis and formability of high-entropy oxides. *J. Mater. Sci.* **2024**, *59* (35), 16618−16628.
(59) Devanathan, V. The Wiedemann-Franz law for electrical and thermal conduction in metals. *J. Chennai Acad. Sci.* **2021**, *3* (1), 1−26.
(60) Galsin, J. S. Heat and Thermodynamics of Solids. In *History of Solid State Physics*; Springer, 2025; pp. 159−179.
(61) Qi, R.; Shi, R.; Li, Y.; Sun, Y.; Wu, M.; Li, N.; Du, J.; Liu, K.; Chen, C.; Chen, J.; et al. Measuring phonon dispersion at an interface. *Nature* **2021**, *599* (7885), 399−403.
(62) Ju, Z.; Chang, Z.; Xiao, N.; Qian, X.; Zhou, Y.; Ma, D. Lattice thermal conductivity of $LiNbO_3$ considering high-order anharmonicity and phonon mutual coherence channel. *Phys. Rev. Appl.* **2025**, *24* (2), 024035.
(63) Gadre, C. A.; Yan, X.; Song, Q.; Li, J.; Gu, L.; Huyan, H.; Aoki, T.; Lee, S.-W.; Chen, G.; Wu, R.; et al. Nanoscale imaging of phonon dynamics by electron microscopy. *Nature* **2022**, *606* (7913), 292−297.
(64) Knijff, L.; Jia, M.; Zhang, C. Electric double layer at the metal-oxide/electrolyte interface. *arXiv*, **2022**, 567, 575.
(65) Kosmulski, M. Compilation of PZC and IEP of sparingly soluble metal oxides and hydroxides from literature. *Adv. Colloid Interface Sci.* **2009**, *152* (1−2), 14−25.
(66) Kosmulski, M. Isoelectric points and points of zero charge of metal (hydr) oxides: 50 years after Parks' review. *Adv. Colloid Interface Sci.* **2016**, *238*, 1−61.
(67) Bellmann, C. Stability of dispersions. *Chem. Eng. Technol.* **2004**, *27* (9), 937−942.
(68) Brown, M. A.; Bossa, G. V.; May, S. Emergence of a stern layer from the incorporation of hydration interactions into the Gouy−Chapman model of the electrical double layer. *Langmuir* **2015**, *31* (42), 11477−11483.
(69) Thomas, R.; Ghosh, D.; Pulimi, M.; Nirmala, J.; Anand, S.; Rai, P. K.; Mukherjee, A. Investigating the transport and colloidal behavior of Fe_3O_4 nanoparticles in aqueous and porous media under varying solution chemistry parameters. *Environ. Sci. Pollut Res. Int.* **2023**, *30* (56), 118693−118705.
(70) Gentili, D.; Ori, G. Reversible assembly of nanoparticles: theory, strategies and computational simulations. *Nanoscale* **2022**, *14* (39), 14385−14432.
(71) dos Santos, R. G. Forces Acting in Colloidal Systems. In *Fundamentals of Surface Thermodynamics: phase Behavior and Its Related Properties*; Springer, 2024.
(72) Wei, X.; Pan, D.; Xu, Z.; Xian, D.; Li, X.; Tan, Z.; Liu, C.; Wu, W. Colloidal stability and correlated migration of Illite in the aquatic environment: The roles of pH, temperature, multiple cations and humic acid. *Sci. Total Environ.* **2021**, *768*, 144174.
(73) Agmo Hernández, V. An overview of surface forces and the DLVO theory. *ChemTexts* **2023**, *9* (4), 10.
(74) Zhang, Y.; Lin, Y.; Li, Y.; Yang, W.; Ye, Y.; Wang, J. Study of stability and aggregation kinetics of coated zero-valent iron nanoparticles. *Desalin. Water Treat.* **2022**, *262*, 298−311.
(75) Ma, E.; Kim, J.; Chang, H.; Ohno, P. E.; Jodts, R. J.; Miller III, T. F.; Geiger, F. M. Stern and diffuse layer interactions during ionic strength cycling. *J. Phys. Chem. C* **2021**, *125* (32), 18002−18014.
(76) Allagui, A.; Benaoum, H.; Olendski, O. On the Gouy−Chapman−Stern model of the electrical double-layer structure with a generalized Boltzmann factor. *Phys. A* **2021**, *582*, 126252.
(77) Bischoff, M.; Kim, N. Y.; Joo, J. B.; Marchioro, A. Water orientation at the anatase TiO_2 nanoparticle interface: A probe of surface pK_a values. *J. Phys. Chem. Lett.* **2022**, *13* (37), 8677−8683.
(78) Yang, X.; Liu, G.; Ma, X.; Xiao, X.; Allangawi, A.; Zhang, H.; Li, W.-L. Cation-and Potential-Dependent Modulation of Hydrophobic Hydration at Electrocatalytic Interfaces. *J. Phys. Chem. C* **2025**, *129* (37), 16958−16966.
(79) Bin Jassar, M.; Yao, Q.; Siro Brigiano, F.; Chen, W.; Pezzotti, S. Chemistry at Oxide/Water Interfaces: The Role of Interfacial Water. *J. Phys. Chem. Lett.* **2024**, *15* (48), 11961−11968.
(80) Tuladhar, A.; Dewan, S.; Pezzotti, S.; Brigiano, F. S.; Creazzo, F.; Gaigeot, M. P.; Borguet, E. Ions Tune Interfacial Water Structure and Modulate Hydrophobic Interactions at Silica Surfaces. *J. Am. Chem. Soc.* **2020**, *142* (15), 6991−7000.
(81) Dai, H.; Han, T.; Cui, J.; Li, X.; Abbasi, H. N.; Wang, X.; Guo, Z.; Chen, Y. Stability, aggregation, and sedimentation behaviors of typical nano metal oxide particles in aqueous environment. *J. Environ. Manage.* **2022**, *316*, 115217.
(82) Shen, Z.; Zhang, Z.; Li, T.; Yao, Q.; Zhang, T.; Chen, W. Facet-Dependent Adsorption and Fractionation of Natural Organic Matter on Crystalline Metal Oxide Nanoparticles. *Environ. Sci. Technol.* **2020**, *54* (14), 8622−8631.
(83) Wang, L.; Shi, C.; Wang, L.; Pan, L.; Zhang, X.; Zou, J. J. Rational design, synthesis, adsorption principles and applications of metal oxide adsorbents: a review. *Nanoscale* **2020**, *12* (8), 4790−4815.
(84) Pan, Z.; Zhu, X.; Satpathy, A.; Li, W.; Fortner, J. D.; Giammar, D. E. Cr (VI) Adsorption on Engineered Iron Oxide Nanoparticles: Exploring Complexation Processes and Water Chemistry. *Environ. Sci. Technol.* **2019**, *53* (20), 11913−11921.
(85) Safir, N. H.; Razlan, Z. M.; Ramasamy, G.; Bakar, S. A.; Abdullah, M. Z. Investigation Of Thermodynamic Properties And Stability Of Metal Oxide (CuO And Al2O3)/Deionized Water Nanofluids For Enhanced Heat Transfer Applications. **2024**. .
(86) Fukasawa, T. Specific Ion Effects in the Handling of Particle Suspensions: A Review. *KONA Powder Part. J.* **2025**, 2026012.
(87) Calis-Ismetoglu, G.; Unal, H. I. Surface engineering of halloysite with graphene oxide via primary and secondary forces, characterizations, and electrokinetic properties. *Mater. Today Commun.* **2023**, *35*, 106101.
(88) Banuelos, J. L.; Borguet, E.; Brown, G. E.; Cygan, R. T.; DeYoreo, J. J.; Dove, P. M.; Gaigeot, M. P.; Geiger, F. M.; Gibbs, J. M.; Grassian, V. H.; et al. Oxide− and Silicate−Water Interfaces and Their Roles in Technology and the Environment. *Chem. Rev.* **2023**, *123* (10), 6413−6544.
(89) Wang, K. Y.; Siboulet, B.; Rébiscoul, D.; Dufrêche, J. F. How Ion Pair Formation Drives Adsorption in the Electrical Double Layer: Molecular Dynamics of Charged Silica-Water Interfaces in the Presence of Divalent Alkaline Earth Ions. *J. Phys. Chem. C* **2021**, *125* (37), 20551−20569.
(90) Derjaguin, B.; Churaev, N.; Muller, V. The Derjaguin−Landau−Verwey−Overbeek (DLVO) theory of stability of lyophobic colloids. In *Surface forces*; Springer, 1987; pp. 293−310.
(91) Zen, A.; Bui, T.; Bao Le, T. T.; Tay, W. J.; Chellappah, K.; Collins, I. R.; Rickman, R. D.; Striolo, A.; Michaelides, A. Long-Range Ionic and Short-Range Hydration Effects Govern Strongly Anisotropic Clay Nanoparticle Interactions. *J. Phys. Chem. C Nanomater Interfaces* **2022**, *126* (18), 8143−8151.
(92) Nakouzi, E.; Kerisit, S. N.; Heo, J.; Legg, B. A.; Sassi, M.; Simonnin, P.; Rosso, K. M. Effect of Ions on Solution Structure and Hydration Forces at the Orthoclase-Water Interface. *J. Phys. Chem. C* **2025**, *129* (15), 7550−7559.

https://doi.org/10.1021/prechem.5c00360
Precis. Chem. XXXX, XXX, XXX−XXX

(93) Butreddy, P.; Heo, J.; Rampal, N.; Liu, T.; Liu, L.; Smith, W.; Zhang, X.; Prange, M. P.; Legg, B. A.; Schenter, G. K.; et al. Ion Correlations Decrease Particle Aggregation Rate by Increasing Hydration Forces at Interfaces. *ACS Nano* **2024**, *18* (38), 26047−26055.
(94) Nakouzi, E.; Kerisit, S.; Legg, B. A.; Yadav, S.; Li, D.; Stack, A. G.; Mundy, C. J.; Chun, J.; Schenter, G. K.; De Yoreo, J. J. Solution Structure and Hydration Forces between Mica and Hydrophilic Versus Hydrophobic Surfaces. *J. Phys. Chem. C* **2023**, *127* (5), 2741−2752.
(95) Liu, M.; Guo, H.; Luo, J.; Gui, X.; Xing, Y.; Cao, Y. Investigation on the effect of metal cation radius on montmorillonite hydration: Combining experiments with molecular dynamics simulation. *Sep. Purif. Technol.* **2025**, *353*, 128474.
(96) Liu, H.; Siani, P.; Bianchetti, E.; Zhao, J.; Di Valentin, C. Multiscale simulations of the hydration shells surrounding spherical Fe_3O_4 nanoparticles and effect on magnetic properties. *Nanoscale* **2021**, *13* (20), 9293−9302.
(97) Sushko, M. L. Driving forces for particle-based crystallization: From experiments to theory and simulations. *MRS Bull.* **2024**, *49* (4), 377−384.
(98) Fan, W.; Zhong, F. Effects of Macroparameters on the Thickness of an Interfacial Nanolayer of Al_2O_3 - and TiO_2 Water-Based Nanofluids. *ACS Omega* **2020**, *5* (43), 27972−27977.
(99) Prasad, T. R.; Krishna, K. R.; Sharma, K. V.; Bhaskar, C. N. Thermal performance of stable SiO_2 nanofluids and regression correlations to estimate their thermophysical properties. *J. Indian Chem. Soc.* **2022**, *99* (6), 100461.
(100) Borzuei, M.; Baniamerian, Z. Role of nanoparticles on critical heat flux in convective boiling of nanofluids: Nanoparticle sedimentation and Brownian motion. *Int. J. Heat Mass Transfer* **2020**, *150*, 119299.
(101) Pochapski, D. J.; Carvalho Dos Santos, C.; Leite, G. W.; Pulcinelli, S. H.; Santilli, C. V. Zeta Potential and Colloidal Stability Predictions for Inorganic Nanoparticle Dispersions: Effects of Experimental Conditions and Electrokinetic Models on the Interpretation of Results. *Langmuir* **2021**, *37* (45), 13379−13389.
(102) Wang, W. T.; Zhang, B. G.; Shi, Y. H.; Zhou, D. K.; Wang, R. Improvement in dispersion stability of alumina suspensions and corresponding chemical mechanical polishing performance. *Appl. Surf. Sci.* **2022**, *597*, 153703.
(103) Murugaiah, D. K.; Shahgaldi, S. Recent progress in understanding the dispersion stability of catalyst ink for proton exchange membrane fuel cell and water electrolyzer. *Int. J. Hydrogen Energy* **2024**, *66*, 156−169.
(104) Li, S.; Yang, H.; Wang, S.; Wang, J.; Fan, W.; Dong, M. Improvement of adsorption and catalytic properties of zeolites by precisely controlling their particle morphology. *Chem. Commun.* **2022**, *58* (13), 2041−2054.
(105) Olarte-Plata, J. D.; Brekke-Svaland, G.; Bresme, F. The influence of surface roughness on the adhesive interactions and phase behavior of suspensions of calcite nanoparticles. *Nanoscale* **2020**, *12* (20), 11165−11173.
(106) Katainen, J.; Paajanen, M.; Ahtola, E.; Pore, V.; Lahtinen, J. Adhesion as an interplay between particle size and surface roughness. *J. Colloid Interface Sci.* **2006**, *304* (2), 524−529.
(107) Blake, T.; De Coninck, J. The influence of solid−liquid interactions on dynamic wetting. *Adv. Colloid Interface Sci.* **2002**, *96* (1−3), 21−36.
(108) Do Hong, S.; Ha, M. Y.; Balachandar, S. Static and dynamic contact angles of water droplet on a solid surface using molecular dynamics simulation. *J. Colloid Interface Sci.* **2009**, *339* (1), 187−195.
(109) Allred, T. P.; Weibel, J. A.; Garimella, S. V. The role of dynamic wetting behavior during bubble growth and departure from a solid surface. *Int. J. Heat Mass Transfer* **2021**, *172*, 121167.
(110) Zhao, P.; Hu, Z.; Cheng, P.; Huang, R.; Gong, S. Coalescence-induced bubble departure: effects of dynamic contact angles. *Langmuir* **2022**, *38* (34), 10558−10567.
(111) Bureš, L.; Sato, Y. On the modelling of the transition between contact-line and microlayer evaporation regimes in nucleate boiling. *J. Fluid Mech.* **2021**, *916*, A53.
(112) Law, K.-Y. Contact angle hysteresis on smooth/flat and rough surfaces. Interpretation, mechanism, and origin. *Acc. Mater. Res.* **2022**, *3* (1), 1−7.
(113) Zhang, F.; Jacobi, A. M. Aluminum surface wettability changes by pool boiling of nanofluids. *Colloids Surf. A* **2016**, *506*, 438−444.
(114) Kim, S. J.; Bang, I. C.; Buongiorno, J.; Hu, L. W. Effects of nanoparticle deposition on surface wettability influencing boiling heat transfer in nanofluids. *Appl. Phys. Lett.* **2006**, *89* (15), 153107.
(115) Wang, J.; Wu, Y.; Cao, Y.; Li, G.; Liao, Y. Influence of surface roughness on contact angle hysteresis and spreading work. *Colloid Polym. Sci.* **2020**, *298* (8), 1107−1112.
(116) Fan, S.; Jiao, L.; Wang, K.; Duan, F. Pool boiling heat transfer of saturated water on rough surfaces with the effect of roughening techniques. *Int. J. Heat Mass Transfer* **2020**, *159*, 120054.
(117) Raghupathi, P. A.; Kandlikar, S. G. Pool boiling enhancement through contact line augmentation. *Appl. Phys. Lett.* **2017**, *110* (20), 204101.
(118) Eral, H. B.; 't Mannetje, D.; Oh, J. M. Contact angle hysteresis: a review of fundamentals and applications. *Colloid Polym. Sci.* **2013**, *291* (2), 247−260.
(119) Barrio-Zhang, H.; Ruiz-Gutiérrez, É.; Armstrong, S.; McHale, G.; Wells, G. G.; Ledesma-Aguilar, R. Contact-angle hysteresis and contact-line friction on slippery liquid-like surfaces. *Langmuir* **2020**, *36* (49), 15094−15101.
(120) Tyowua, A. T.; Yiase, S. G. Contact angle hysteresis−advantages and disadvantages: a critical review. *Prog. Adhes. Adhes.* **2021**, *6*, 47−67.
(121) Forsberg, P. S. H.; Priest, C.; Brinkmann, M.; Sedev, R.; Ralston, J. Contact line pinning on microstructured surfaces for liquids in the Wenzel state. *Langmuir* **2010**, *26* (2), 860−865.
(122) Gurganus, C. W.; Charnawskas, J. C.; Kostinski, A. B.; Shaw, R. A. Nucleation at the contact line observed on nanotextured surfaces. *Phys. Rev. Lett.* **2014**, *113* (23), 235701.
(123) Herbaut, R.; Dervaux, J.; Brunet, P.; Royon, L.; Limat, L. A criterion for the pinning and depinning of an advancing contact line on a cold substrate. *Eur. Phys. J. Spec. Top.* **2020**, *229* (10), 1867−1880.
(124) Dupuy, A. D.; Chellali, M. R.; Hahn, H.; Schoenung, J. M. Multiscale phase homogeneity in bulk nanocrystalline high entropy oxides. *J. Eur. Ceram. Soc.* **2021**, *41* (9), 4850−4858.
(125) Tomboc, G. M.; Zhang, X.; Choi, S.; Kim, D.; Lee, L. Y. S.; Lee, K. Stabilization, Characterization, and Electrochemical Applications of High-Entropy Oxides: Critical Assessment of Crystal Phase−Properties Relationship. *Adv. Funct. Mater.* **2022**, *32* (43), 2205142.
(126) Usharani, N. J.; Shringi, R.; Sanghavi, H.; Subramanian, S.; Bhattacharya, S. Role of size, alio-/multi-valency and non-stoichiometry in the synthesis of phase-pure high entropy oxide (Co, Cu, Mg, Na, Ni, Zn) O. *Dalton Trans.* **2020**, *49* (21), 7123−7132.
(127) Chellali, M. R.; Sarkar, A.; Nandam, S. H.; Bhattacharya, S. S.; Breitung, B.; Hahn, H.; Velasco, L. On the homogeneity of high entropy oxides: An investigation at the atomic scale. *Scr. Mater.* **2019**, *166*, 58−63.
(128) Gwalani, B.; Martin, A.; Kautz, E.; Guo, B.; Lambeets, S.; Olszta, M.; Battu, A. K.; Malakar, A.; Yang, F.; Guo, J.; et al. Mechanistic understanding of speciated oxide growth in high entropy alloys. *Nat. Commun.* **2024**, *15* (1), 5026.
(129) Gambinossi, F.; Mylon, S. E.; Ferri, J. K. Aggregation kinetics and colloidal stability of functionalized nanoparticles. *Adv. Colloid Interface Sci.* **2015**, *222*, 332−349.
(130) Kallay, N.; Žalac, S. Stability of nanodispersions: a model for kinetics of aggregation of nanoparticles. *J. Colloid Interface Sci* **2002**, *253* (1), 70−76.
(131) Cai, J.; Zhu, H. Surface-engineered nanostructured high-entropy alloys for advanced electrocatalysis. *Commun. Mater.* **2025**, *6* (1), 118.

https://doi.org/10.1021/prechem.5c00360
Precis. Chem. XXXX, XXX, XXX−XXX

(132) Yin, Z.-Q.; Li, X.-F.; Bao, F.-B.; Tu, C.-X.; Gao, X.-Y. Thermophoresis and Brownian motion effects on nanoparticle deposition inside a 90 square bend tube. *Aerosol Air Qual. Res.* **2018**, *18* (7), 1746−1755.
(133) Kulkarni, P.; Biswas, P. A Brownian dynamics simulation to predict morphology of nanoparticle deposits in the presence of interparticle interactions. *Aerosol Sci. Technol.* **2004**, *38* (6), 541−554.
(134) Albojamal, A.; Vafai, K. Analysis of particle deposition of nanofluid flow through porous media. *Int. J. Heat Mass Transfer* **2020**, *161*, 120227.
(135) Ruo, A.-C.; Chang, M.-H. Effect of gravity settling on the onset of thermal convection in a nanofluid-saturated porous medium layer. *J. Fluid Mech.* **2024**, *984*, A5.
(136) Ghazivini, M.; Hafez, M.; Ratanpara, A.; Kim, M. A review on correlations of bubble growth mechanisms and bubble dynamics parameters in nucleate boiling. *J. Therm. Anal. Calorim.* **2022**, *147* (11), 6035−6071.
(137) Piazza, R. Thermophoresis: moving particles with thermal gradients. *Soft Matter* **2008**, *4* (9), 1740−1744.
(138) Karthikeyan, C.; Kalpana, G.; Krishnamoorthy, V.; Samuel, A. A. Transient numerical analysis of thermophoresis and particle dynamics in a nanofluid−pool boiling conditions. *J. Mol. Liq.* **2020**, *301*, 112459.
(139) Putnam, S. A.; Cahill, D. G.; Wong, G. C. Temperature dependence of thermodiffusion in aqueous suspensions of charged nanoparticles. *Langmuir* **2007**, *23* (18), 9221−9228.
(140) Rozati, S. A.; Khriwish, M. B.; Gupta, A. Speleothem-Inspired Copper/Nickel Interfaces for Enhanced Liquid−Vapor Transport by Marangoni and Soret Effects. *Langmuir* **2024**, *40* (20), 10745−10758.
(141) Tadros, T. Electrostatic and steric stabilization of colloidal dispersions. *Electr. Phenom. Interfaces Biointerfaces* **2012**, 153−172.
(142) Roos, N. Entropic forces in Brownian motion. *Am. J. Phys.* **2014**, *82* (12), 1161−1166.
(143) Abdolzadeh, M.; Mehrabian, M. Combined effect of thermophoretic force and other influencing parameters on the particle deposition rate on a tilted rough surface. *Int. J. Therm. Sci.* **2011**, *50* (6), 954−964.
(144) Gupta, S. K.; Misra, R. D. Experimental pool boiling heat transfer analysis through novel ZnO-coated Cu (Cu@ZnO nanoparticle) hybrid nanofluid boiling on the fin tops of different microchannels. *J. Therm. Anal. Calorim.* **2023**, *148* (21), 12247−12267.
(145) Sharma, P. O.; Barewar, S. D.; Chougule, S. S. Experimental investigation of heat transfer enhancement in pool boiling using novel Ag/ZnO hybrid nanofluids. *J. Therm. Anal. Calorim.* **2021**, *143* (2), 1051−1061.
(146) Pare, A.; Ghosh, S. K. Surface qualitative analysis and ANN modelling for pool boiling heat transfer using Al_2O_3-water based nanofluids. *Colloids Surf. A* **2021**, *610*, 125926.
(147) Moghadasi, H.; Saffari, H. Experimental study of nucleate pool boiling heat transfer improvement utilizing micro/nanoparticles porous coating on copper surfaces. *Int. J. Mech. Sci.* **2021**, *196*, 106270.
(148) Gao, Y.; Hsieh, H. E.; Zhang, Z. B.; Wang, S. Q.; Zhou, Z. Experimental study on pool boiling heat transfer characteristics of TiO2 nanofluids on a downward-facing surface. *Prog. Nucl. Energy* **2022**, *153*, 104402.
(149) Du, J.; Yang, W.; Zhu, H.; Wang, J.; Cao, Z.; Sunden, B. Experimental study of pool boiling performance of Fe_3O_4 ferromagnetic nanofluid on a copper surface. *Appl. Therm. Eng.* **2024**, *248*, 123213.
(150) Wang, S.; Hsieh, H.-E.; Zhang, Z.; Wang, S.; Cai, X. CHF and heat transfer enhancement by SiO_2 nanofluids on a inclined downward facing heating surface. *Prog. Nucl. Energy* **2024**, *171*, 105197.
(151) Yagnem, A. R.; S, V. Heat transfer enhancement studies in pool boiling using hybrid nanofluids. *Thermochim. Acta* **2019**, *672*, 93−100.
(152) Kathiravan, R.; Kumar, R.; Gupta, A.; Chandra, R. Preparation and pool boiling characteristics of copper nanofluids over a flat plate heater. *Int. J. Heat Mass Transfer* **2010**, *53* (9−10), 1673−1681.
(153) Kamel, M. S.; Lezsovits, F. Experimental Investigation on Pool Boiling Heat Transfer Performance Using Tungsten Oxide WO_3 Nanomaterial-Based Water Nanofluids. *Materials* **2020**, *13* (8), 1922.
(154) Chopkar, M.; Das, A. K.; Manna, I.; Das, P. K. Pool boiling heat transfer characteristics of ZrO_2−water nanofluids from a flat surface in a pool. *Heat Mass Transfer* **2008**, *44* (8), 999−1004.
(155) Kim, J.; Jun, S.; Laksnarain, R.; You, S. M. Effect of surface roughness on pool boiling heat transfer at a heated surface having moderate wettability. *Int. J. Heat Mass Transfer* **2016**, *101*, 992−1002.
(156) Jones, B. J.; McHale, J. P.; Garimella, S. V. The Influence of Surface Roughness on Nucleate Pool Boiling Heat Transfer. *J. Heat Trans.-Trans. ASME* **2009**, *131* (12), 121009.
(157) Balsamy-Kamaraj, A.; Hasan, M. M.; Merugu, S.; Gupta, A. Comparison of 3D-printed copper surfaces for enhanced pool boiling heat transfer. *Manuf. Lett.* **2025**, *44*, 1649−1656.
(158) Rozati, S. A.; Gupta, A. Enhanced Phase Change Heat Transfer with Fused Deposition Modeling (FDM) Printed Pit and Pillar (Pi2) Arrays. *Exp. Therm. Fluid Sci.* **2025**, *161*, 111337.
(159) Rozati, S. A.; Keesara, P.; Mahajan, C.; Mondal, K.; Gupta, A. Magnetically aligned metal-organic deposition (MOD) ink based nickel/copper heater surfaces for enhanced boiling heat transfer. *Appl. Therm. Eng.* **2022**, *211*, 118473.
(160) Rishi, A. M.; Rozati, S. A.; Trybus, C.; Kandlikar, S. G.; Gupta, A. Investigation of structure-property-boiling enhancement mechanisms of copper/graphene nanoplatelets coatings. *Front. Mech. Eng.* **2021**, *7*, 642214.
(161) Mukherjee, A.; Kandlikar, S. G. Numerical study of single bubbles with dynamic contact angle during nucleate pool boiling. *Int. J. Heat Mass Transfer* **2007**, *50* (1−2), 127−138.
(162) Kim, M.; Kim, S. J. A mechanistic model of critical heat flux for pool boiling based on supply failure mechanisms depending on the contact angle. *Int. J. Heat Mass Transfer* **2023**, *209*, 124090.
(163) Donahue, N. D.; Kanapilly, S.; Stephan, C.; Marlin, M. C.; Francek, E. R.; Haddad, M.; Guthridge, J.; Wilhelm, S. Quantifying chemical composition and reaction kinetics of individual colloidally dispersed nanoparticles. *Nano Lett.* **2022**, *22* (1), 294−301.
(164) Dor, S.; Rühle, S.; Ofir, A.; Adler, M.; Grinis, L.; Zaban, A. The influence of suspension composition and deposition mode on the electrophoretic deposition of TiO2 nanoparticle agglomerates. *Colloids Surf. A* **2009**, *342* (1−3), 70−75.
(165) Chong, M. Y.; Numan, A.; Liew, C. W.; Ramesh, K.; Ramesh, S. Comparison of the performance of copper oxide and yttrium oxide nanoparticle based hydroxylethyl cellulose electrolytes for supercapacitors. *J. Appl. Polym. Sci.*, **2017**, *134*, 13, .
(166) da Silva Cardoso, R.; de Amorim, S. M.; Scaratti, G.; Moura-Nickel, C. D.; Moreira, R. P. M.; Puma, G. L.; Moreira, R. D. F. P. M. Structural, optical and photocatalytic properties of erbium (Er 3+) and yttrium (Y 3+) doped TiO 2 thin films with remarkable self-cleaning super-hydrophilic properties. *RSC Adv.* **2020**, *10* (29), 17247−17254.
(167) Sutton, C.; Levchenko, S. V. First-Principles Atomistic Thermodynamics and Configurational Entropy. *Front Chem.* **2020**, *8*, 757.
(168) Lombardo, S.; Gencer, A.; Schutz, C.; Van Rie, J.; Eyley, S.; Thielemans, W. Thermodynamic Study of Ion-Driven Aggregation of Cellulose Nanocrystals. *Biomacromolecules* **2019**, *20* (8), 3181−3190.
(169) Elakiyaasokan, V. K.; Kalyanaraman, G.; Nagarajan, N. G. Aqueous Solubility Enhancement and Thermodynamic Aggregation Behavior of Resveratrol Using an Eco-Friendly Hydrotropic Phenomenon. *Russ. J. Phys. Chem. A* **2019**, *93* (13), 2681−2686.
(170) Peidys, D. A.; Santiago, A. A. H.; Evstigneev, M. P. The interplay of enthalpic/entropic factors in nanoparticles' aggregation in solution: The case of fullerene C. *J. Mol. Liq.* **2020**, *318*, 114043.
(171) Sundar, L. S.; Singh, M. K.; Sousa, A. C. M. Investigation of thermal conductivity and viscosity of Fe3O4 nanofluid for heat

transfer applications. *Int. Commun. Heat Mass Transfer* **2013**, *44*, 7−14.
(172) Begum Elcioglu, E.; Murshed, S. M. Ultrasonically tuned surface tension and nano-film formation of aqueous ZnO nanofluids. *Ultrason. Sonochem.* **2021**, *72*, 105424.
(173) Rohsenow, W. M. A method of correlating heat-transfer data for surface boiling of liquids. *Trans. Am. Soc. Mech. Eng.* **1952**, *74* (6), 969−975.
(174) Zuber, N. *Hydrodynamic Aspects Of Boiling Heat Transfer (Thesis)*; Ramo-Wooldridge Corp.: CA (United States); Univ. of California: Los Angeles, 1959. DOI:

https://doi.org/10.1021/prechem.5c00360
Precis. Chem. XXXX, XXX, XXX−XXX